Reductive Coupling of Nitric Oxide by Cu(I): Stepwise Formation of Mono and Dinitrosyl Species *en route* to a Cupric Hyponitrite Intermediate

Mayukh Bhadra,[†§*] Therese Albert,[‡] Alicja Franke,[χζ] Verena Josef,[χ] Ivana Ivanović-Burmazović,[χζ] Marcel Swart,[⊥Ψ] Pierre Moënne-Loccoz[‡*] and Kenneth D. Karlin[†*]

[†]Department of Chemistry, The Johns Hopkins University, Baltimore, Maryland 21218, United States

[‡]Department of Chemical Physiology and Biochemistry, Oregon Health & Science University, Portland, Oregon 97239, United States

[⊥]IQCC & Departament de Química, Universitat de Girona, Campus Montilivi (Ciencies), 17003 Girona, Spain

[Ψ]ICREA, Pg. Lluís Companys 23, 08010 Barcelona, Spain

[χ]Department of Chemistry and Pharmacy, Friedrich-Alexander University Erlangen-Nuremberg, 91058 Erlangen, Germany

[ζ]Department of Chemistry, Ludwig-Maximilians University, Munich, 81377 Munich, Germany

KEYWORDS. Nitric oxide, Reductive coupling, Hyponitrite, Isomerization, Mononitrosyl, Dinitrosyl, Nitrous oxide, Resonance Raman, Stopped-flow kinetics, Disproportionation, Computational Analyses (DFT).

ABSTRACT: Transition metal-mediated reductive coupling of nitric oxide ($NO_{(g)}$) to nitrous oxide ($N_2O_{(g)}$) has significance across the fields of industrial chemistry, biochemistry, medicine, and environmental health. Herein, we elucidate a DFT-supplemented mechanism of $NO_{(g)}$ reductive coupling at a copper-ion center $[(tmpa)Cu^{I}(MeCN)]^+$ (**1**) {tmpa = tris(2-pyridylmethyl)amine}. At −110 ^{0}C in EtOH (<−90^{0}C in MeOH), exposing 1 to $NO_{(g)}$ leads to a new binuclear hyponitrite intermediate $[\{(tmpa)Cu^{II}\}_2(\mu\text{–}N_2O_2^{2-})]^{2+}$ (**2**), exhibiting temperature-dependent irreversible isomerization to the previously characterized κ^2-O,O'-trans-$[(tmpa)_2Cu_2^{II}(\mu\text{–}N_2O_2^{2-})]^{2+}$ (***OO*^{Xray}**) complex. Complementary stopped-flow kinetic analyses of the reaction in MeOH reveals an initial mononitrosyl species $[(tmpa)Cu(NO)]^+$ (**1-(NO)**) that binds a second NO molecule forming a dinitrosyl species $[(tmpa)Cu^{II}(NO)_2]$ (**1-(NO)$_2$**). The decay of **1-(NO)$_2$** requires available starting complex **1** to form a dicopper-dinitrosyl species hypothesized to be $\{(tmpa)Cu\}_2(\mu\text{-}NO)_2]^{2+}$ (**D**) bearing a diamond-core motif, en route to the formation of hyponitrite intermediate **2**. In contrast, exposing **1** to $NO_{(g)}$ in 2-MeTHF:THF (v/v 4:1) at <−80 °C leads to the newly observed transient metastable dinitrosyl species ($[(tmpa)Cu^{II}(NO)_2]$ (**1-(NO)$_2$**), prior to its disproportionation-mediated transformation to the nitrite product $[(tmpa)Cu^{II}(NO_2)]^+$. Our study furnishes a near-complete profile of $NO_{(g)}$ activation at a reduced Cu site with tripodal tetradentate ligation, in two distinctly different solvents, aided by detailed spectroscopic characterization of metastable intermediates, including Resonance Raman characterization of the new dinitrosyl and hyponitrite species detected.

INTRODUCTION

Nitric oxide ($NO_{(g)}$) plays a ubiquitous role as a signaling molecule and an essential regulator for neural transmission, inhibitor of platelet aggregation, and modulator of apoptosis, -repair of wounds and cellular proliferation.[1-6] Regulated levels of $NO_{(g)}$ strengthen the mammalian host defense response by effecting oxidative destruction of harmful pathogen biomolecules (i.e., by oxidation and/or nitration) as elevated levels of $NO_{(g)}$ cause degradation of essential proteins, lipids and nucleic acids.[5, 7-12] Toxic overproduction of $NO_{(g)}$ and reactive NO_x products such as peroxynitrite ($^-$OONO) and nitrogen dioxide (NO_2) are mitigated by the oxidation of $NO_{(g)}$ to NO_3^- by iron-containing metalloenzymes.[7-8, 10, 13] In anoxic conditions, microbial organisms will resort to the reductive degradation of toxic $NO_{(g)}$ through Fe/Cu-mediated reductive coupling of two $NO_{(g)}$ to benign $N_2O_{(g)}$.[14-23] This critical reaction **2 NO$_{(g)}$ + 2H$^+$ + 2e$^-$ → N$_2$O$_{(g)}$ + H$_2$O** is also an essential step in denitrification, of the geochemical nitrogen cycle, and in the effective detoxification of automotive and industrial exhausts by catalytic convertors.[24-28]

Microbial nitric oxide reductase (NOR) activity is displayed mainly by three sets of $NO_{(g)}$ reduction enzymes: 1) the denitrifying heme/non-heme $NO_{(g)}$ reductases,[16, 18, 23, 25, 29-30] as well as some heme/copper NO reducing terminal oxidases (HCOs),[30-35] 2) the flavin-dependent $NO_{(g)}$ reductase possessing a non-heme diiron active site,[14, 20-22, 36-38] and 3) the fungal P450nors with heme-thiolate active sites enzymes.[39] At this time, the catalytic mechanism adopted by P450nors seems broadly accepted: it includes the formation of a ferric heme-nitrosyl adduct prone to 2-electron reduction by NADH to form an iron-nitroxyl (i.e., HNO) intermediate that reacts with a second NO to produce N_2O and to regenerate the ferric protein.[40-41] In enzymes with binuclear active sites, reductive coupling of $NO_{(g)}$ is thought to involve two key steps: i) N–N bond formation between two metal-nitrosylated reduced units forming a hyponitrite anion ($N_2O_2^{2-}$, **HN**) and ii) N–O bond scission from the **HN** intermediate to release

$N_2O_{(g)}$.[14, 18, 29, 42-48] Although enzymatic studies and model chemistries have provided useful mechanistic insights, there remains a great deal of ambiguity around the order and timing of transfer of electrons from the metal centers to $NO_{(g)}$, formation and coordination modes of the M–NO unit (end-on, κ^1–O, κ^1–N; side-on, κ^2–O,N) and M-**HN** (cis, trans, monoanionic, dianionic, neutral) moieties and the timing and pathway of proton-shuttling events.[48-52]

The functional role of Cu in the activation of $NO_{(g)}$ has long been explored in both protein studies related to HCOs and model complexes.[23] Cu-mediated $NO_{(g)}$-activation and coupling is also significant to our understanding of a) Cu-dependent nitrite reductases that transform $NO_{(g)}$ to $N_2O_{(g)}$ under high $[NO_{(g)}]$,[18] b) $Cu^I/NO_{(g)}$-disproportionation reactions that generate $N_2O_{(g)}$ and NO_2^-,[53-58] c) peroxynitrite formation by Cu-superoxo species[59-60] and d) NOx absorption and environmental detoxification.[28, 53, 61] In our own efforts to understand reductive coupling of $NO_{(g)}$ at a Cu-chelate model, we isolated the structurally characterized κ^2-O,O'-*trans*-$[L_2Cu_2^{II}(\mu\text{–}N_2O_2)^{2-})]^{2+}$ complex (***OO*^{xray}**) by subjecting stoichiometric or excess amounts of $NO_{(g)}$ to $[(tmpa)Cu^I(MeCN)]^+$ {tmpa = tris(2-pyridylmethyl)amine} (**1**) in protic MeOH at RT and demonstrated a solvent (protic vs aprotic)-dependent difference in $NO_{(g)}$ activation products.[62] Metal bound κ^2-O,O'-*trans*-μ–$N_2O_2^{2-}$ units have also been observed in synthetic Fe,[44, 63-65] Co,[66] and Y[67] systems, and shown to yield quantitative $N_2O_{(g)}$ upon acidic proton-dependent N–O bond cleavage.[68] In contrast, κ^2-O,O'-*cis*-$N_2O_2^{2-}$ binding geometries has been observed in Ru[69] and Ni[70-73] model systems and Warren and coworkers most recently structurally characterized an overall anionic ligand copper(II)-**HN** complex with *cis*-O,O'-binding (with Cu(I) ligations one **HN** N-atom), which yields N_2O upon acidification.[74] Recently, we also demonstrated how a second-sphere H-bonding derived H^+ transfer facilitates N–O bond cleavage of ***OO*^{xray}** to release $N_2O_{(g)}$, underscoring the crucial balance between H-bonding capabilities and acidities in (bio)chemical $NO_{(g)}$ coupling systems.[75] Nonetheless, there remain huge uncertainties concerning the reaction pathway leading to formation of the κ^2-O,O'-$N_2O_2^{2-}$ unit and a comprehensive mechanistic description of Cu-mediated $NO_{(g)}$ reductive coupling is still far-fetched.

In this article, we elucidate details of solvent-dependent reaction pathways for the reductive-coupling (and/or disproportionation) chemistry of $NO_{(g)}$ reactivity with $[(tmpa)Cu^I(MeCN)]^+$ (**1**) (**Figure 1**). Spectroscopic (UV-Vis and resonance Raman) monitoring of the solvent and temperature dependence of the NO reductive coupling reaction aided by low-temperature stopped-flow kinetics and computational analysis, lead to the characterization of two new intermediates, including a cupric dinitrosyl species **1**-$(NO)_2$ and a dicupric-hyponitrite species **2** with novel **HN** coordination geometry distinctly different from that of the *trans*-μ-*O*,*O*'-hyponitrite dicopper(II) complex characterized by X-ray crystallography (***OO*^{xray}**);[62] and to which it subsequently isomerizes to in MeOH.[62]

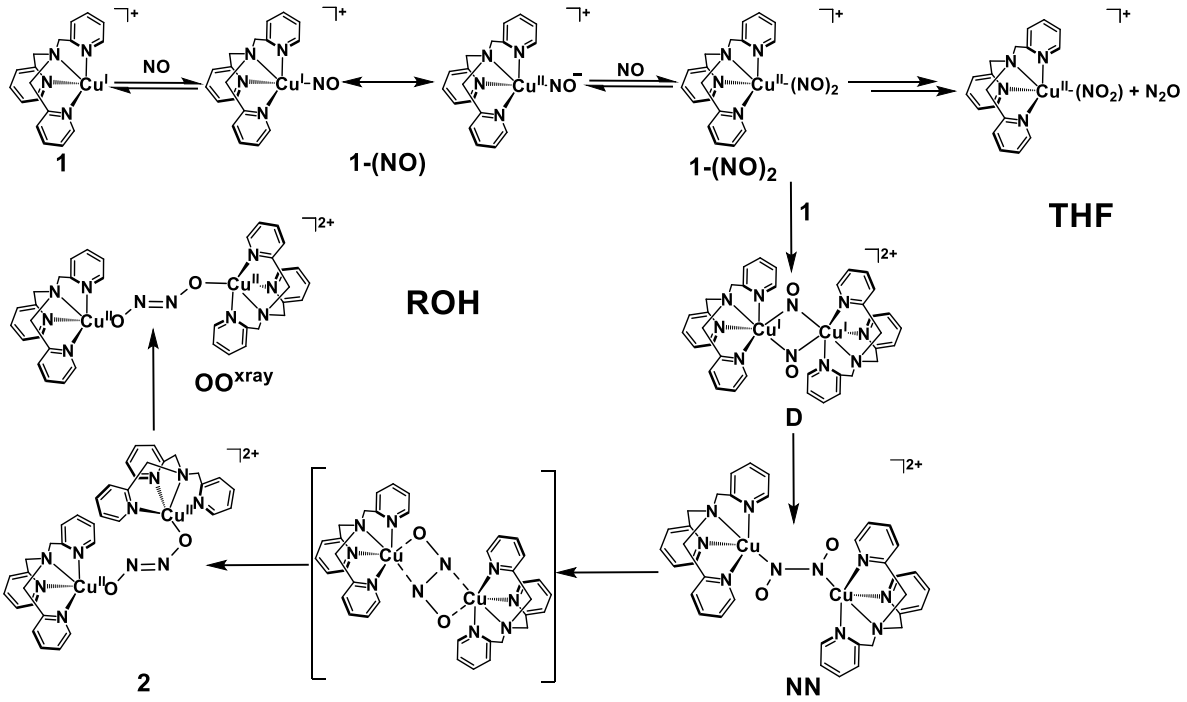

Figure 1. The overall scheme for the reductive coupling of $NO_{(g)}$ in MeOH and the disproportionation of $NO_{(g)}$ in THF solvents facilitated by $[(tmpa)Cu^I(MeCN)]^+$ (**1**). See the text for detailed discussion on the intermediates involved.

RESULTS AND DISCUSSION

Prior work has shown that room temperature exposure of **1** to $NO_{(g)}$ in MeOH generates the structurally characterized ***OO*^{xray}** complex while the same reaction performed in THF leads to the disproportionation-mediated nitrite-product $[(tmpa)Cu^{II}(NO_2)]^+$.[62] As mentioned, we present considerably advanced insights, including the finding of new intermediates, via the low-temperature exploration of these reactions.

A green mononuclear *dinitrosyl* intermediate, 1-(NO)$_2$. Introduction of $NO_{(g)}$ to a pre-chilled yellow solution of **1** between −80 °C and −145 °C in 2-MeTHF:THF mixture (4:1 v/v) produces a brilliant green intermediate (See **Figure 2**) with an intense absorption band at 340 nm (ε = 8000 M^{-1} cm^{-1}) and distinctive 630 nm feature (ε = 600 M^{-1} cm^{-1}) and very weak transitions observed at 830 nm (ε = 100 M^{-1} cm^{-1}) and 915 nm (ε = 100 M^{-1} cm^{-1}) prior to its disproportionation to the Cu^{II}-NO_2^- product (UV-Vis; 410 nm, 840 nm) (**Figure S1**), which occurs in this solvent (but not in ROH, see below).[62]Notably, this intermediate exhibiting the 630 nm band is stable at −145 °C for at least ~20-30 minutes and only slowly transforms to the Cu^{II}-NO_2^- product over a period of >3 hours when heated to −135 °C (see **Figure S2**). The Cu^{II}-NO_2^- product $[(tmpa)Cu^{II}(NO_2)]^+$, also verified by Griess test, is formed in near-quantitative yield (95%, **Figure S1**) and the disproportionation-mediated $N_2O_{(g)}$ generated is obtained at ~78% yield (see the GC Data section in the SI), as has also been observed in similar systems.[76]

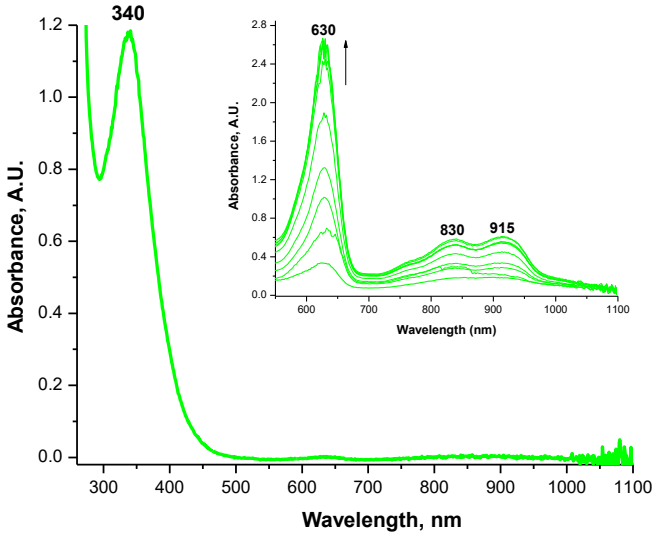

Figure 2. UV-Vis spectrum of the green intermediate species (the putative dinitrosyl-copper complex **1-(NO)$_2$**, *vide infra*) formed after addition of $NO_{(g)}$ to a 0.15 mM solution of **1** at −145 °C in 2-MeTHF:THF (4:1 v/v) (green trace); the inset shows the formation of the 630 nm feature of the intermediate with additional weak bands at 830 nm and 915 nm immediately following the addition of excess $NO_{(g)}$ to a 5.0 mM solution of **1** at −145 °C in 2-MeTHF:THF (4:1 v/v).

The identity of this green intermediate was investigated by resonance Raman (RR) spectroscopy; exposing **1** to $NO_{(g)}$, $^{15}NO_{(g)}$, and $^{15}N^{18}O_{(g)}$ at −80 °C and freezing the samples within less than a minute as the color of the solutions evolved from yellow to green. RR spectra obtained with a 647 nm excitation show intense bands at 1364 and 1622 cm^{-1} that shift with NO-isotope substitutions (**Figure 3**), and match expectation for isotope sensitivity of ν(N-O) modes (**Table 1**). The two ν(NO)s are suggestive of a Cu-dinitrosyl complex **1-(NO)$_2$**, and are accompanied by low-frequency bands at 768, 666, 585, and 510 cm^{-1} consistent with Cu-N-O stretching and bending vibrations. Furthermore, RR data obtained with a mixture of ^{14}NO and $^{15}N^{18}O$ gases show new bands with intermediate frequencies between the ν($^{15}N^{18}O$) and ν(N-O) modes which supports a description of the two ν(N-O) modes as coupled vibrations, i.e., symmetric and asymmetric vibrations (see **Figure S3**). Varying the Cu(I) starting concentration and incubation time before freezing affects the intensity of these RR bands relative to solvent bands, but the relative intensities of all these NO-isotope sensitive bands are retained, supporting their assignment to a single species with absorption features as seen in the UV-Vis data (**Figure 2**).

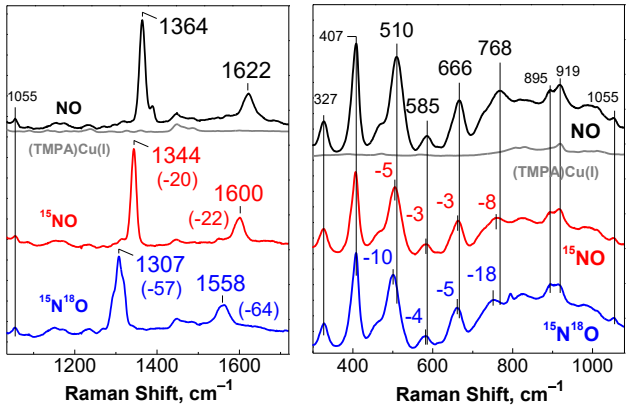

Figure 3. RR spectra of (**1-(NO)$_2$**) in 4:1 MeTHF:THF mixture measured at 110 K with a 647-nm laser excitation and generated with unlabeled NO (black), ^{15}NO (red), and $^{15}N^{18}O$ (blue); also shown is the spectrum of **1** obtained in the same conditions (grey).

The low-frequency RR modes are reminiscent of symmetric and asymmetric ν(N-Fe-N) and δ(N-Fe-N) in dinitrosyl-iron complexes (DNICs) but are upshifted by ~100 cm^{-1} as may be expected from a $\{M(NO)_2\}^{12}$ or $\{M(NO)_2\}^{13}$ species. Inversely, the ν(N-O) are observed at much lower frequencies than in $\{Fe(NO)_2\}^9$ and $\{Fe(NO)_2\}^{10}$ DNICs (see **Table 1** below).[76-77] In DNICs, the higher N-O stretching frequency is the more intense RR signal and is assigned to the symmetric ν_s(N-O), but in the complex characterized here, the low-frequency ν(N-O) is the more intense band. Also, while differences between symmetric and asymmetric N-O stretches (i.e., Δν(N-O)) range between 10 and 100 cm^{-1} in DNICs and reflect differences in metal coordination numbers and ON-Fe-NO angles, the Δν(NO) observed here is 258 cm^{-1}, suggesting a $Cu^{II}(NO)(NO^-)$ electronic

configuration with strong *d* to π* backbonding leading to high Cu-N-O stretching/bending frequencies and low N-O stretches. There are mentions of Cu-dinitrosyl species in Cu-zeolite catalysts and argon matrix studies,[78-79] but we are not aware of any report for copper-dinitrosyl complexes in homogeneous systems. As a relevant aside, EPR measurements on green **1-(NO)$_2$** indicated this species is EPR-silent as expected (see the SI **Figure S4**).[80]

Table 1. Vibrational frequencies of **1-(NO)$_2$** and DNICs[a]

	(tmpa)Cu(NO)$_2$ ($\Delta^{15}N$, $\Delta^{18}O$)	{(SPh)$_2$Fe(NO)$_2$}^{9}	{(TMEDA)Fe(NO)$_2$}^{10}
ν(N-O)s	**1622** (-22, -*64*) **1364** (-20, -*56*)	1731sym (-37) 1692asym (-31)	1687 (-35) 1630 (-34)
νas(N-M-N)	**768** (-8, -*18*)	598 (-4)	n.r.
νs(N-M-N)	**666** (-3, -5)	525 (-6)	n.r.
δs(N-M-N)	**585** (-3, -*4*)	440 (-11)	n.r.
δas(N-M-N)	**510** (-5, -*10*)	n.r.	n.r.

[a]Frequences in cm^{-1}; ^{15}NO and ^{15}N^{18}O shifts are reported in parentheses; n.r., not reported.

A brown binuclear *trans*-hyponitrite intermediate, 2. In striking contrast to the THF-chemistry (*vide supra*), addition of excess NO$_{(g)}$ to a pre-chilled solution of **1** at −110 °C in EtOH leads to the generation of a stable brown species **2** with a strong absorption feature at 470 nm (ε ~ 1600 M^{-1}cm^{-1}) and additional low-energy bands at 630 and 825 nm (ε ~ 370 and 480 M^{-1}cm^{-1}, respectively) (**Figure 4**). Full conversion of **1** to **2** requires ~2-3 hours at −110 °C and **2** is stable for > 4 hours in solution. This hyponitrite species [{(tmpa)Cu^{II}}$_2$(N$_2$O$_2^{2-}$)]$^{2+}$ (**2**) (see below) is directly generated upon mixing **1** and xs NO$_{(g)}$ in MeOH at −95 °C.

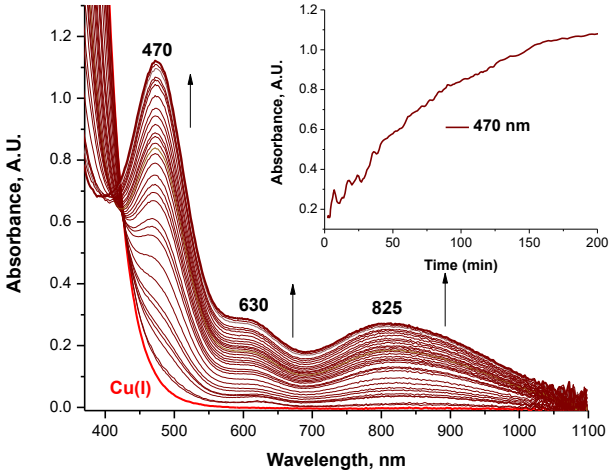

Figure 4. UV-Vis spectra of the reaction of [(tmpa)Cu^{I}(MeCN)]$^+$ (**1**, red trace) with excess NO$_{(g)}$ at −110 °C in EtOH showing the growth of the 470, 630 and 825 nm absorption features (brown trace) of the putative hyponitrito intermediate [{(tmpa)Cu^{II}}$_2$(N$_2$O$_2^{2-}$)]$^{2+}$ (**2**) (inset) time course of the growth of the 470 nm band.

Monitoring the decay of **2** at temperatures between – 85 and –50 °C by UV-Vis spectroscopy shows the gradual loss of the 470 nm band of **2** in favor of absorption bands at 312 (ε ~ 3800 M^{-1}cm^{-1}), 670 (ε ~ 200 M^{-1}cm^{-1}) and 875 nm (ε = 270 M^{-1}cm^{-1}) that match those of the previously structurally characterized and RT stable κ^2-O,O'-*trans*-[(tmpa)$_2$Cu$_2^{II}$(N$_2$O$_2$)$^{2-}$)]$^{2+}$ (***OO^{xray}***; see **Figure 1**) complex (**Figure 5**). Cooling ***OO^{xray}*** to −110 °C does not regenerate the absorption spectrum of **2**, providing experimental evidence for the greater thermal stability of ***OO^{xray}*** compared to **2**. Addition of excess NO$_{(g)}$ to a solution of **1** in EtOH at room temperature directly yields the green ***OO^{xray}*** complex, indicating the general stability of ***OO^{xray}*** in ROH solvents at room temperature.[62]

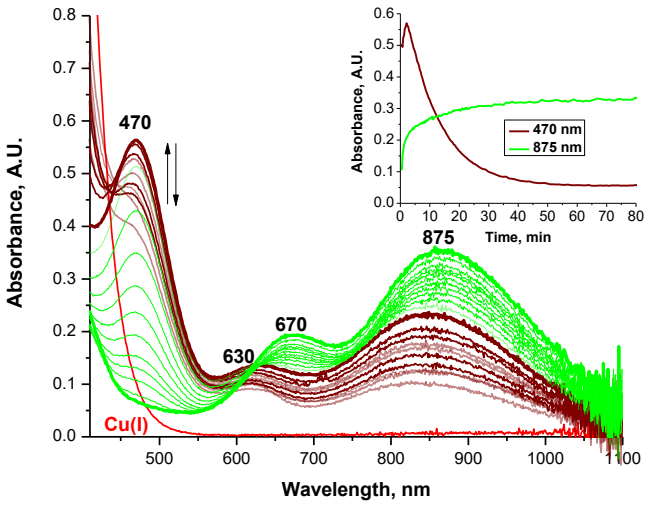

Figure 5. UV-Vis spectra of the reaction of **1** (1 mM) with excess NO$_{(g)}$ at −50 °C in EtOH, showing the rapid formation of **2** (brown trace) from the starting complex **1** (red trace) in solution and the decay of **2** (brown trace) to ***OO^{xray}*** (green trace). The time traces of the 470 nm and 875 nm bands are shown in inset.

RR spectra of **2** obtained with a 458 nm laser excitation show intense bands that downshift when the intermediate is prepared with ^{15}NO$_{(g)}$ and ^{15}N^{18}O$_{(g)}$ (**Figure 6**). A strong band at 1393 cm^{-1} that downshifts 47 cm^{-1} with ^{15}NO and ^{15}N^{18}O is assigned to a ν(N=N) since this value matches the calculated ^{15}N-downshift from Hooke's law for a harmonic N–N oscillator. Additional features at 1117 and 1164 cm^{-1} that show both ^{15}N- and ^{18}O-isotope sensitivity are assigned to ν$_s$(N-O) and ν$_{as}$(N-O) modes, respectively. A band at 581 cm^{-1} that shifts –31 cm^{-1} with ^{15}N^{18}O but is unaffected by ^{15}NO labeling is assigned to the in-plane δ(ONNO) mode. The lack of sensitivity of the ν(N=N) to ^{18}O-labeling and that of the δ(ONNO) to ^{15}N-labeling support a symmetric coordination geometry of the bridging **HN** ligand, i.e. *μ*-κ^2-N,N'-*trans* or *μ*-κ^2-O,O'-*trans* bridging geometry, where N- and O-atoms displacements are restricted to N=N stretch and O-NN-O bend, respectively.

A band at 375 cm^{-1} that shifts –2 and –8 cm^{-1} with ^{15}NO and ^{15}N^{18}O may correspond to a ν(Cu-N$_2$O$_2$) or an out-of-plane δ(ONNO) deformation mode (**Figure 6**). Other low-frequency RR bands at 316,

456, and 484 cm^{-1} show no isotope sensitivity and must correspond to vibrations from the tmpa ligand; our DFT calculations (*vide infra*) confirm all these assignments, including the 375 cm^{-1} band as the out-of-plane δ(ONNO) mode, and the other low-frequency RR bands as tmpa vibrations. These data represent the first RR characterization of a cupric-hyponitrito species. Importantly, RR experiments with ***OO*^{xray}** in EtOH or MeOH at room temperature or −110 ^{0}C with laser excitation at 647 or 407 nm revealed no resonance-enhanced signals, as reported previously.[47, 62, 75]

Raman data for metal-hyponitrito ($ONNO^{2-}$) species are scarce but a thorough comparison of the vibrational frequencies obtained for **2** to that of $Na_2N_2O_2$ in H_2O and μ-*N*,*O*-hyponitrite bis[pentaamine-Co(III)]$^{4+}$ cation undoubtedly establishes the presence of a bidentate *trans*-$ONNO^{2-}$ unit in **2** (**Table 2**)[81-82] the likely structure of which is discussed below.

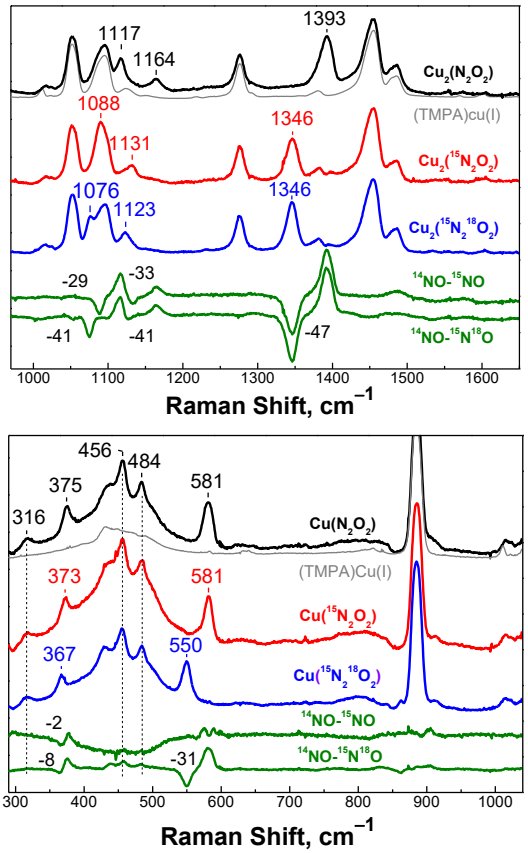

Figure 6. RR spectra of **2** prepared in EtOH at −110 ^{0}C and measured at 110 K with a 458 nm laser excitation and generated with unlabeled NO (black), ^{15}NO (red), and $^{15}N^{18}O$ (blue); also shown are the spectrum of **1** obtained in the same conditions (grey), and the isotope-edited difference spectra (green traces).

Table 2. Comparison of the vibrational frequencies (in cm^{-1}) of **2** with those of $[(NH_3)_5(Co(III)]_2(ONNO^{2-})$ μ-N^3,O^1, the free hyponitrite ($ONNO^{2-}$) anion[81-82] and DFT calculated values (vide infra).

	[(tmpa)Cu]$_2$(ONNO) {i.e. 2}(Δ^{15}N, Δ^{18}*O*)	DFT calculated frequencies for **2.EtOH$_4$** (*vide infra*) **(Δ^{15}N, Δ^{18}*O*)**	$[(NH_3)_5Co]_2(ONNO^{2-})$ μ-N^1,O^1 (Δ^{15}N)	$ONNO^{2-}$ (Δ^{15}N)
ν(N-N)	**1393 (-47, *0*)**	1376 (-45, *0*)	1391 (-43)	1390 (-46)
$\nu(N\text{-}O)_{as}$	**1164 (-33, -8)**	1068 (-27, -33)	1124 (-28)	1119 (-28)
$\nu(N\text{-}O)_s$	**1117(-29, -*12*)**	1021 (-26, -9)	1033 (-20)	
			916 (-11)	
δ(ONNO)	**581 (0, -*31*)**	545 (-4, -*15*)	600 (0)	684 (-2)
	375 (-2, -8)	411 (-4, -*16*)	372 (-7)	
		243 (-5, -2)	323 (-1)	
			238 (-3)	

The EPR spectrum of **2** also supports a symmetric bridging geometry of the **HN** ligand since an excellent fit of these experimental data can be obtained using a single set of g and A values; these EPR parameters are characteristic of a classic reverse axial-like pattern as expected for a d_z^2 ground state within a trigonal bipyramid (TBP) copper(II) ion geometry (**Figure 7**). This EPR spectrum thus also indicates that the Cu(II) centers are magnetically isolated, supporting a lack of exchange coupling through the **HN** group bridging the two Cu(II) ions. Such observations were also found with the ***OO*^{xray}** complex,[62] and a close analogue.[75]

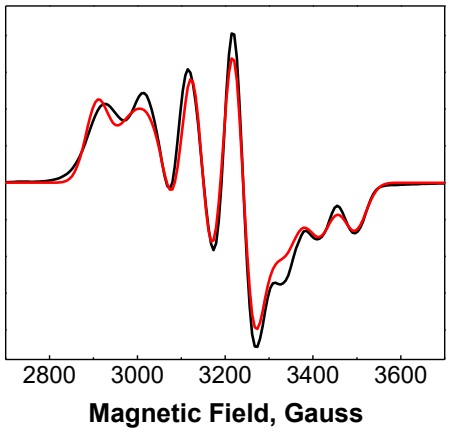

Figure 7. EPR spectrum of $[\{(tmpa)Cu^{II}\}_2(N_2O_2^{2-})]^{2+}$ (**2**) (2 mM in MeOH/EtOH = 1:1 glass) at 20 K (black trace) and simulated spectrum (g = 2.19, 2.16, 1.99; A = 326, 236, 214 MHz) (red trace), indicating the copper(II) ions in **2** possess trigonal bipyramidal geometries and are magnetically isolated (see text).

Low-temperature stopped-flow kinetic analysis of the formation of 1-(NO)$_2$ and 2 in MeOH. Stopped-flow UV-Vis experiments conducted with different concentrations of **1** (0.5 – 2 mM) and $NO_{(g)}$ (0.175 – 7 mM) in MeOH at −85 °C provide information on the reaction leading to the formation of **1-(NO)$_2$** and **2** (**Figure 8**). A first intermediate, evidenced by appearance of an absorption feature at 627 nm in the first 45 ms of the reaction (before it loses intensity) performed with the lowest NO concentration (0.175 mM) is tentatively assigned to a $[(tmpa)Cu^{I}(NO)]^+$ complex **1-(NO)** (**Figure 9**). At all

other $NO_{(g)}$ concentrations, this growth phase is not observed and only it decays to a new species with much weaker absorbance in the ~620 and 400 nm region of the visible spectrum.

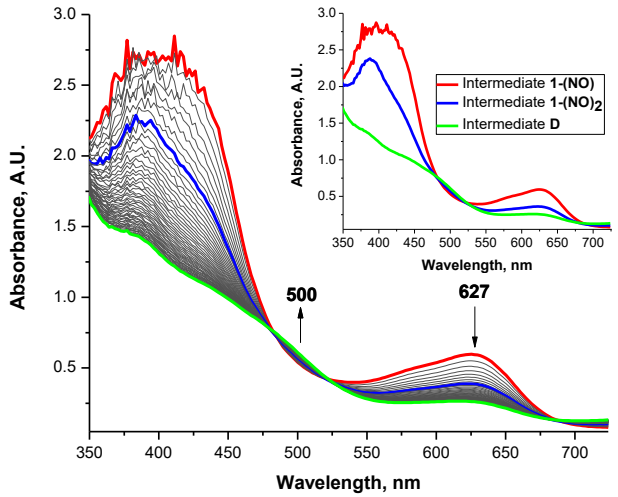

Figure 8. Rapid-scan spectra recorded within 0.001 to 0.5 s of the reaction of **1** (1 mM) and $NO_{(g)}$ (3.5 mM) in MeOH at –85 °C (first and last spectra (red and green traces, respectively), intermediate spectrum with maximum **1-(NO)$_2$** contribution (blue trace); Inset: simulated spectra of **1-(NO)** (red), **1-(NO)$_2$** (blue) and **D** (green) from the global analysis of the decay of **1-(NO)**.

Experiments performed at different $NO_{(g)}$ concentrations show that the decay rate of **1-(NO)** increases with increasing $NO_{(g)}$ concentrations (**Figure 9, inset**). These data may reflect binding of a second $NO_{(g)}$ molecule to **1-(NO)** to form a dinitrosyl derivative or an accelerated dimerization of **1-(NO)** at higher $NO_{(g)}$ concentrations due to a larger fraction of **1-(NO)**. Further kinetic experiments allow us to exclude the latter alternative. Specifically, determining the fraction of **1-(NO)** produced at different $NO_{(g)}$ concentrations shows that **1-(NO)** saturates at $[NO_{(g)}]$ = 0.7 mM and 1 mM (L)Cu^I while its decay rate continues to increase at 3.5 mM $NO_{(g)}$. For more mechanistic details see the SI and **Figure S5**.

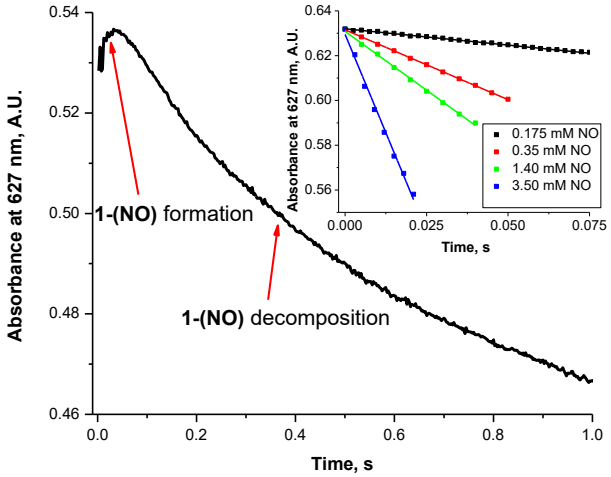

Figure 9. Kinetic trace for the reaction of **1** (1 mM) with $NO_{(g)}$ (0.175 mM) in MeOH at –85 °C showing the buildup of **1-(NO)** within the first 45 ms. Inset: initial rates for the decomposition of **1-(NO)** (1 mM) under varying $NO_{(g)}$ concentrations; to better visualize this comparison of decomposition rates, starting absorbance and starting decay time were adjusted for each $NO_{(g)}$ concentrations to account for the impact of these different $NO_{(g)}$ concentrations on the formation rate and maximum concentration buildup of **1-(NO)**.

Using the initial rate method with varying $NO_{(g)}$ concentrations, the conversion of **1-(NO)** is shown to be a first-order process with respect to $NO_{(g)}$ (n = 1.0 ± 0.2, see **Figure S6**). Thus, species **1-(NO)** reacts with $NO_{(g)}$ to form a copper-dinitrosyl complex $[(L)Cu^{I}(NO)_2]^+$ or $[(L)Cu^{II}(NO^-)(NO)]^+$ (**1-(NO)$_2$**). Accordingly, the optical features (blue spectrum, **Figure 8**) observed by stopped-flow in MeOH agree reasonably well with those of **1-(NO)$_2$** in aprotic solvent (**see Figure 2**). Importantly, the formation of this copper-dinitrosyl complex is observed even at sub-stoichiometric concentration of $NO_{(g)}$ showing that this species is thermodynamically favorable relative to its mononitrosyl precursor ($K_2 > K_1$), a characteristic often seen with iron chemistry of NO.[83-87]

Although **1-(NO)$_2$** is clearly formed at low [NO] it does not accumulate in the reaction mixture and undergoes subsequent conversion to a new species within the next 2 seconds. At higher $NO_{(g)}$ concentration, i.e. [NO] = 7 mM, the formation and decay/transformation of intermediate **1-(NO)** is too fast to be observed, but the formation of **1-(NO)$_2$** is well resolved and reveals a pseudo-first rate constant k_{obs} = 7.3 ± 0.2 s^{-1} at –85 °C and [NO] = 7 mM (**Figures S7 and S8**). Unfortunately, the very rapid decay of **1-(NO)$_2$** at [NO] > 7 mM precluded the determination of a second-order rate constant. Nevertheless, assuming a steady state concentration of **1-(NO)** and negligible back reaction, the second-order rate constant for the formation of **1-(NO)$_2$** can be approximated to be 1050 ± 30 $M^{-1}s^{-1}$ at –85 °C in MeOH (**Figure 10**).

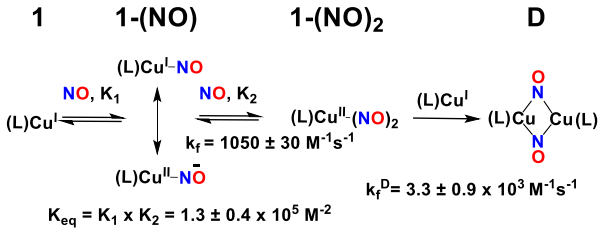

Figure 10. Proposed sequential pathway and kinetic parameters for the formation of **1-(NO)**, **1-(NO)$_2$** and putative dicopper-dinitrosyl intermediate **D** in the reaction of $NO_{(g)}$ with **1** at –85 °C in MeOH.

Importantly, the decay of **1-(NO)$_2$** occurs with its fastest rate at moderate concentration of NO ([NO] = 3.5 mM, i.e. 1.5-fold relative to **1**) (**Figure S9**), indicating that it requires the presence of unreacted complex **1** to form a dicopper-dinitrosyl intermediate we name **D**. Although the kinetic description of the formation of **1-(NO)$_2$** and its decay product are complex, a rigorous kinetic analysis provides an overall equilibrium constant for the formation of **1-(NO)$_2$** (**1** + 2 NO = **1-**

(NO)$_2$), $K_{(NO)2}$ = 1.3 ± 0.4 x 10^5 M^{-2}, and a second order rate constant for the formation of the intermediate **D**, k_f^D= 3.3 ± 0.9 x 10^3 $M^{-1}s^{-1}$ (see more details of the kinetic analysis in pages **S9-S13** and **Figures S10 and S11** in Supporting Information).

On the longer time scale intermediate **D** decomposes to a transient species we name **NN** that displays an absorption band at 460 nm before proceeding to several new species with spectral characteristics (470 nm) resembling those of intermediate **2** (**Figures 11 and S12**).

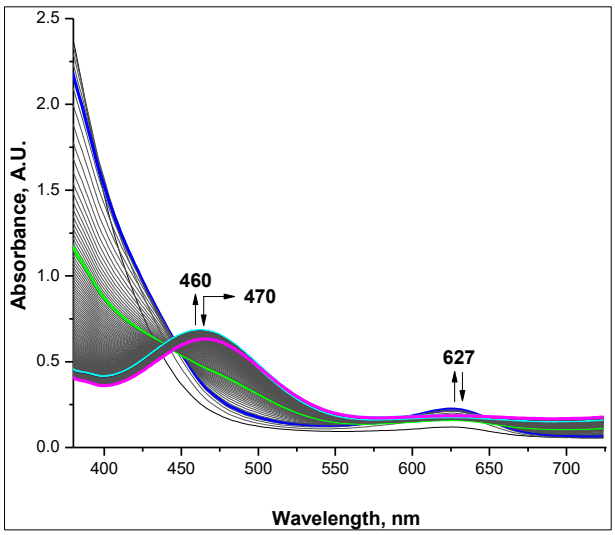

Figure 11. Rapid-scan spectra recorded for the reaction of 1 mM (L)Cu^I and 7 mM $NO_{(g)}$ in MeOH at -85 °C within 25 seconds showing the transition from intermediate **1-(NO)$_2$** with its characteristic 627-nm absorption (blue trace), to intermediates **D** (unfeatured visible absorption, green trace), **NN** (460-nm maximum, cyan trace) and **2** (470-nm maximum, magenta trace).

Computational (DFT) analyses. DFT calculations were carried out at the S12g/TZ2P level,[88-89] as recently accomplished in successful fashion for antiferromagnetically coupled diiron^{III} and diiron^{IV} complexes.[90] The calculated electronic structure (Figures **S13-S14**) for the mononitrosyl complex **1-(NO)** (See pages **S17-S18**) shows the copper atom remaining in the reduced Cu^I state exhibiting a distorted TBP geometry, and the radical character remaining fully localized on the nitrosyl ligand (i.e., the MDC-d spin-density charges on NO sum up to 1.02 electrons). This finding is consistent with those determined for other Cu(I)-derived mononitrosyl species in literature.[53-55] The Cu–N(nitrosyl) distance (Table **5.1.2**, **SI**) is found at 1.91 Å, significantly shorter than the Cu–N(tmpa) distances found between 2.06 and 2.18 Å. The N–O distance at 1.20 Å is halfway between that observed (at CCSD(T)/aug-cc-pVQZ) for a NO radical (1.15 Å) and a nitroxyl moiety (i.e., NO^-) (1.25-1.26 Å). Accordingly, the computed NO stretching frequency (Table **5.1.3**, **SI**) in **1-(NO)** is 1596 cm^{-1}, significantly lower than the NO stretch of free NO at 1908 cm^{-1} (NO radical, S12g/TZ2P).[91] This value is also lower than those observed for other Cu-NO species.[53-55] The Cu–N–O angle is observed at 119.9° (Figure **S13**, **SI**), which is consistent with a nitrosyl double bond as confirmed by the BODSEP bond order of 1.95 (Table **5.1.2**, **SI**) and the lower absorption frequency. Cu-NO structures in a square pyramidal environment and with O-coordination were also tested computationally and found to be less stable (see pages **S19-S25**).

Binding of a second $NO_{(g)}$ to **1-(NO)** might lead to a $[(L)Cu^I(NO)_2]^+$ or a $[(L)Cu^{II}(NO^-)(NO)]^+$ electronic structure for **1-(NO)$_2$** (See pages **S27-S34**). DFT calculations produce Cu^I and Cu^{II} electronic structures that are isoenergetic with Gibbs free energies that only differ by less than 1 kcal·mol^{-1} (Table **5.2.1, SI**). The Cu^I description (**C^{altA1}**, see Figure **S25**, Tables **5.2.2-5.2.3** in the **SI**) favors covalently bound nitrosyl groups to form a hyponitrite moiety (O–N=N–O) with NO stretches at 1369 and 1451 cm^{-1}, close to nitroxyl anions species. This dianion character would suggest a Cu^{III} state if it were not for an inverse ligand field,[92] and indeed the orbital occupations indicate a Cu^I state.

The Cu^{II} description (see **Figure 12** and **C^3**, Figures **S30-S31**), with an N–N bond only partially formed, as indicated by a N–N distance of 2.08 Å (Table **5.2.6** in the **SI**) and BODSEP bond order of 0.46 ((Table **5.2.6** in the **SI**), shows radical character on the copper, and NO stretches at 1538 cm^{-1}, 1726 cm^{-1} (**Figure 3**, **Table 1**) that are more consistent with nitrosyl radical than nitroxyl anions. These calculated frequencies are quite high relative to experimental values for **1-(NO)$_2$**, but they produce a Δν(NO)s of 188 cm^{-1} (Table **5.2.7** in the **SI**) that matches better the 258 cm^{-1} value observed in the RR spectra of **1-(NO)$_2$** (**Table 1**). The computed UV-Vis spectrum of the Cu^{II} structure with intense peaks between 375-400 nm, shoulder around 480 nm and a minor peak at 666 nm (see Figures **S26, S29, S32**) is a closer match to the experimental data for **1-(NO)$_2$** (**Figure 2**). Efforts to model structures of **1-(NO)$_2$** in square pyramidal geometries showed these to not be viable; see further comments in the SI (see pages **S34-S55**).

As described above, the next intermediate **D** evidenced by the stopped-flow analysis corresponds to the addition of a cuprous ion complex to the dinitrosyl species **1-(NO)$_2$**. The DFT modeling for this intermediate supports a $Cu_2(NO)_2$ diamond core structure (**Figures 1, S56**),[93] as most recently described by S. Zhang and coworkers[93a] and also similar to a recent motif found in iron-nitrosyl chemistry.[93b] Our calculations (see pages **S56-S57**) indicate a Cu^I oxidation state with dissociation of one pyridine ring per copper (Cu-N distance 3.01 Å)(**Tables 5.3.1-5.3.2** in the **SI**) to facilitate the formation of the diamond core with pentacoordinate Cu^I centers (Figure **12**).

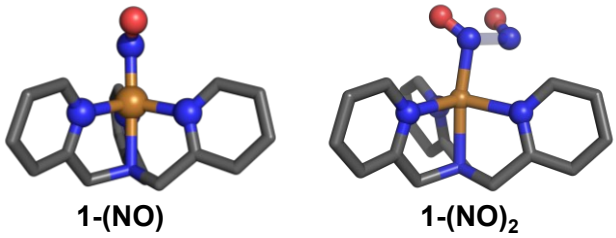

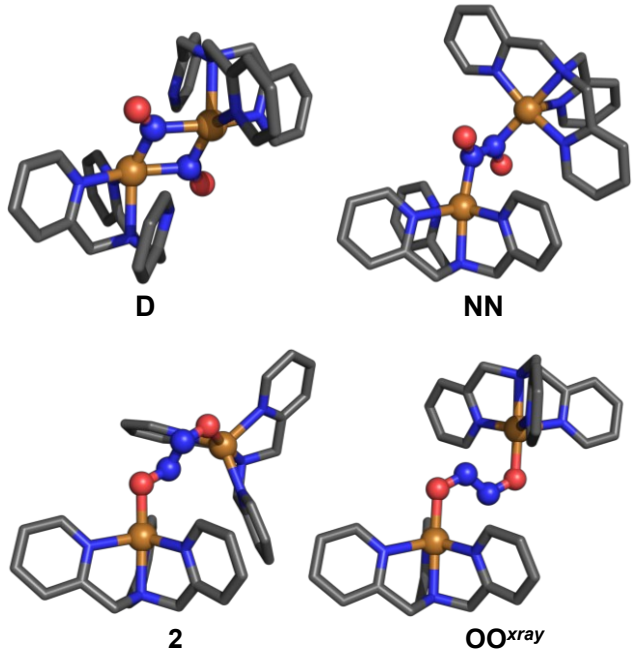

Figure 12. DFT optimized structures for intermediates **1-(NO)** - ***OO*^{xray}** based on calculations at (COSMO, ZORA)-S12g/TZ2P. See the text and Supporting Information for additional details.

The subsequent formation of the N–N bond is accompanied by the breaking of diamond core, leading to a dicopper(II)-hyponitrite intermediate **NN**, the proposed N,N' bound hyponitrite (see Section **5.4** in the **SI**; Pages **S58-S64**), prior to rotation of the hyponitrite to form the first O,O-bound hyponitrito dicopper(II) complex **2**, characterized by resonance Raman spectroscopy (**Figure 1**). Based on the structure of **NN**, a counter-clockwise rotation in which the oxygen atoms bind to the opposite copper seems to be the most plausible route to formation of **2**. In the formation of this species (see Supporting Information, pages **S65-S70**), the two tmpa ligands are oriented in a *cis*-like manner, possibly stabilized through π-π stacking of pyridine rings from opposite tmpa ligands (Figures **S67-S68**). The weakly anti-ferromagnetically coupled Cu^{II} in intermediate **2** are bonded to the **HN** moiety in the axial position (**Figure 13**) with Cu–O distances of 1.949/1.991 Å (see Table **5.5.1** in the **SI**). Importantly, the symmetry around the hyponitrite ligand in **2** produces calculated vibrational frequencies and N/O isotope shifts that match observed RR frequencies (**Table 2** in main text and Table **5.5.2** in the **SI**). This match is particularly true when four solvent molecules are included explicitly in the calculations for intermediate **2**, bringing the computed ν(N–N) values of the proposed structure **2•EtOH$_4$** at 1376 cm^{-1} and $\Delta^{15}N$ and $\Delta^{18}O$ shifts in perfect agreement with experiments (see Supporting Information, Tables **5.5.3-5.5.4**; pages **S68-S70**). The in-plane and out-of-plane δ(ONNO) frequencies (at 545 and 411 cm^{-1} with DFT, respectively; Table **5.5.4**. in the **SI**) also produce isotope shifts that match the RR data. The computed trigonal bipyramidal coordination of the two Cu(II) ion is also consistent with the observed EPR spectrum of **2** (**Figure 7**).

Rotation of one of the tmpa ligands in **2** suffices to bring the overall structure of the dicopper complex towards the trigonal bipyramidal structure in the room temperature stable hyponitrito complex ***OO*^{xray}** observed previously by X-ray crystallography.[62] The N–N central distance of 1.273 Å in **2** (Table **5.5.1** in the **SI**) is only slightly larger than that observed in ***OO*^{xray}** (1.257 Å X-ray;[62] 1.270 Å DFT (Table **5.6.1** in the **SI**)), while the N–O distance is somewhat larger in the X-ray structure (1.360 Å) than by DFT (1.310/1.325 Å for **2**, 1.310 Å for ***OO*^{xray}** (Table **5.6.1** in the **SI**)). Although no MeOH molecules was found in the crystal structure of **OO^{xray}**,[62] the inclusion of four explicit solvent molecules in the calculations improves the agreement significantly, with N–O distances of 1.334/1.342 for **2•EtOH$_4$** and 1.318/1.329 Å for ***OO*^{xray}•EtOH$_4$**, and N–N central distances of 1.259 Å for **2•EtOH$_4$** and 1.260 Å for ***OO*^{xray}•EtOH$_4$** (see Supporting Information, pages **S68-S70** for computational details of **2•EtOH$_4$**, **S74-S76** for computational details of ***OO*^{xray}•EtOH$_4$**).

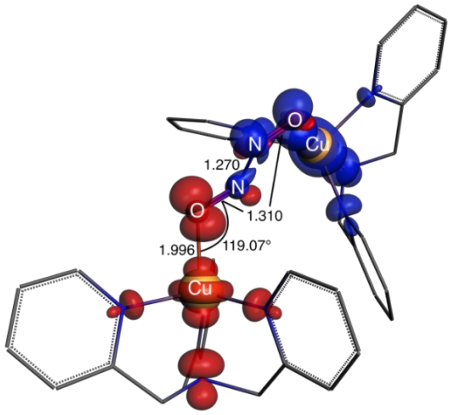

Figure 13. (COSMO/ZORA)S12g/TZ2P optimized structure of **2** and its spin-density (isosurface value 0.005). An alternative computational structure includes four EtOH solvent molecules which are H-bonded to the hyponitrito ligand. See the text and Supporting Information for additional details.

Additionally, the Gibbs free energies for structures **D** to ***OO*^{xray}** (**Figure 12**) are all within a < 5 kcal·mol^{-1} range, which corroborates the viability of the proposed reaction path. These differences are even smaller when four solvent molecules are included explicitly. Because of the large size of the system involved, no transition-state searches have yet been attempted.

Reactivity studies of intermediate 2. Exposing **2** to 1-10 equiv of the O-atom scavengers viz. Me_2S and Ph_3P at −110 ^{0}C had no measurable effect. Similarly, **2** did not react with Lewis acids such as $Sc(OTf)_3$, $Zn(OTf)_2$ or weaker Bronsted acids such as *p*-cyanophenol and *p*-nitrophenol. However, exposure of **2** to 1 equiv of the strong acid $[H(DMF)]^+(^-OTf)$ results in a 50% loss of the 470-nm absorption feature from **2** and complete loss after addition of 2 equiv of the acid (**Figure 14**) over a period of 50 minutes. GC analysis of the reaction vessel headspace reveals a near-quantitative production of $N_2O_{(g)}$ (~85%) (**Figure S79**).

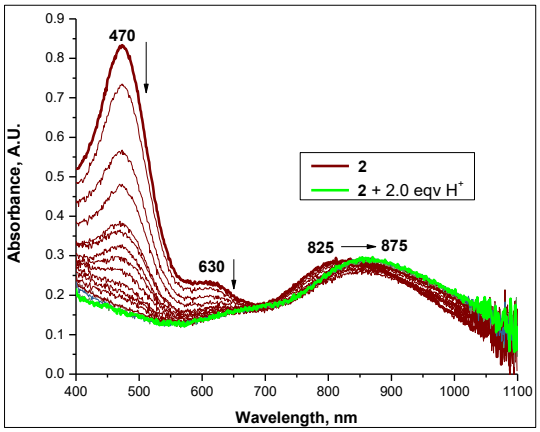

Figure 14. UV-Vis spectroscopic monitoring of reaction of **2** with two equiv $[H(DMF)]^+(^-OTf)$ at −110 °C. Complete decay of the 470 nm band takes 50 minutes.

CONCLUSION

Our study provides a detailed mechanism of Cu-mediated $^{\bullet}NO_{(g)}$ reductive coupling in protic/H-bonding alcohol solvents. For copper ion systems where initial reaction of a Cu(I)-complex with $NO_{(g)}$ is exceedingly fast, we have provided evidence for the formation of an initial mononuclear copper-nitrosyl unit, whereupon a new cupric dinitrosyl intermediate **1-(NO)$_2$** is identified for the first time by resonance Raman spectroscopy. Efforts to model this intermediate by DFT produced a number of isoenergetic cupric structures, which only moderately reproduce the spectroscopic features of **1-(NO)$_2$**. The dinitrosyl species converts to a novel cupric hyponitrite intermediate characterized again for the first time by resonance Raman spectroscopy. DFT modeling of this complex **2** produces an excellent match in vibrational frequencies supporting a κ^2-O,O'-*trans*-$[L_2Cu_2^{II}(N_2O_2)^{2-})]^+$ structure. Complex **2** isomerizes at higher temperatures to a symmetric O, O'-*trans*-hyponitrito complex ***OO^{xray}***. These data represent the first concrete example of a temperature-dependent isomerization of a metal-bound hyponitrite species *en route* to N-O bond cleavage. Strikingly, the hyponitrite formation is only achieved in H-bond donating solvents (R-OH), with the mononuclear-dinitrosyl intermediate **1-(NO)$_2$** decomposing to the nitrite product $[(tmpa)Cu^{II}(NO_2)]^+$ in aprotic tetrahydrofuran. This solvent dependence supports a crucial role for hydrogen bond interactions in facilitating N–N bond formation in dinitrosyl species.[94] Future synthetic model studies incorporating intramolecular H-bond donors are already underway in our laboratories.

EXPERIMENTAL SECTION

Materials and Methods. All commercially available chemicals were purchased at the highest available purity from either Sigma-Aldrich (Millipore Sigma) or TCI America and were used as received unless otherwise stated. Synthesis and manipulation of air-/moisture-sensitive substances were carried out using standard Schlenk techniques under an argon atmosphere, or in a nitrogen-filled Vacuum Atmospheres glovebox with H_2O and O_2 levels <1 ppm. All organic solvents were purchased at HPLC-grade or better. Methanol/Ethanol were degassed (bubbling argon gas for 40 min at room temperature) in an addition funnel connected to an evacuated Strauss flask under an inert atmosphere and dried using molecular sieves after transferring to the glovebox. All solvents were then stored in dark glass bottles inside the glovebox over 3 Å activated molecular sieves for at least 72 hrs prior to use. Nitric oxide was purchased from Matheson Gases and purified according to published procedures.[95-97] Purified $NO_{(g)}$ was then stored in 25 or 50 mL Schlenk flasks sealed with a rubber spectrum and copper wire. $^{15}N^{16}O$ and $^{15}N^{18}O$ bottles (1 litre) were both purchased from ICON Isotopes (Dexter, MI) and transferred directly to individual 25 ml Schlenk flasks using air-free techniques.

Instrumentation. UV-Vis absorption spectra were collected on a Cary-50 Bio spectrophotometer equipped with a liquid nitrogen chilled Unisoku USP-203-A cryostat (Unisoku Scientific Instruments) using a 1 cm modified Schlenk cuvette. Electron paramagnetic resonance (EPR) spectra were collected in 5 mm (outer diameter) quartz tubes using an X-band Bruker EMX-plus spectrometer coupled to a Bruker ER 041 XG microwave bridge (~9.4 GHz) and a Bruker EMX 081 power supply: microwave frequency = 9.42 GHz, microwave power = 0.201 mW, attenuation = 30 dB, modulation amplitude = 10 G, modulation frequency = 100 kHz, temperature = 20 K. Gas chromatographic analysis for headspace $N_2O_{(g)}$ quantification was carried out using a Agilent 8860 instrument (manual injection) equipped with a HP-5 {specifications: 30 m long, 0.32 mm wide (with a 0.25 μm film)} J&W GC capillary column. The GC samples were injected using a 100 μL gas-tight syringe, and the injector oven and detector oven were maintained at 200 and 300 °C respectively. The GC column temperature was set at 150 °C. The duration of each GC experiment was 10 min.

Stopped-Flow Kinetics. All experiments were performed using a Biologic cryo SFM-4000 four-syringe stopped-flow combined with a 150 W xenon lamp and a J&M TIDAS diode array detector (200–724 nm, integration time 0.5 ms). Prior to use, the stopped-flow system was flushed two times with argon and two times with degassed methanol. For the measurements only two syringes were used. The solutions of $NO_{(g)}$ and Cu^I(tmpa)complex were mixed in a 1:1 ratio with a total flow rate of 5.5 mL/s, resulting in a total volume of 226 μL. For cooling a Huber C-905 cryostat filled with silicon oil was used. The analyses of spectral changes as well as global analysis of kinetic traces at various wavelengths were performed by the use of Specfit, Global Analysis System (Version 3.0.38 for 32-bit Windows system).

All solutions were prepared in degassed methanol as solvent under anaerobic conditions. $NO_{(g)}$ saturated solution was prepared by bubbling pure $NO_{(g)}$ gas through methanol in Schlenk tube equipped with septum (usually 10 mL of methanol was bubbled for 20 minutes). NO gas was purified in accordance with literature procedures (saturated potassium hydroxide, column of Ascarite, column of P_2O_5).[98] The concentration of the saturated $NO_{(g)}$ solution in methanol was determined by a NO-sensitive electrode (14 mM). For the different $NO_{(g)}$ concentrations, appropriate dilutions of NO saturated solution were performed by using a Hamilton gastight syringe equipped with a 3-way valve. The solutions of Cu^I(tmpa) complex were prepared and stored in the glovebox and brought outside by using Hamilton gastight syringes equipped with 3-way valves.

Computational details. All DFT calculations were performed with the Amsterdam Density Functional (ADF)[99-100] and QUILD[101] programs. Molecular orbitals were expanded in an uncontracted set of

Slater type orbitals (STOs) of triple-ζ quality with double polarization functions (TZ2P).[102-103] Core electrons were not treated explicitly (frozen core approximation[100]). An auxiliary set of s, p, d, f, and g STOs was used to fit the molecular density and to represent the Coulomb and exchange potentials accurately for each SCF cycle. Geometries were optimized with the QUILD[101] program using adapted delocalized coordinates until the maximum gradient component was less than 10^{-4} a.u. Energies, gradients, Hessians[104] (for vibrational frequencies) and UV-Vis spectra (TD-DFT) were calculated with the S12g functional,[88-89] by including solvation effects through the COSMO[105] dielectric continuum model with appropriate parameters for the solvents.[106] For computing Gibbs free energies, all small frequencies were raised to 100 cm^{-1} in order to compensate for the breakdown of the harmonic oscillator model.[107-108] Scalar relativistic corrections have been included self-consistently in all calculations by using the zeroth-order regular approximation (ZORA)[109]. For the frequencies calculations the Becke[110-111] grid of Normal quality was used; all other S12g calculations were performed with a Becke grid of VeryGood quality. All DFT calculations were performed using the unrestricted Kohn-Sham scheme.

All computational data have been uploaded (DOI: 10.19061/iochem-bd-4-35) onto the IOCHEM-BD platform (www.iochem-bd.org) to facilitate data exchange and dissemination, according to the FAIR principles[112] of OpenData sharing.

Samples for UV-Vis study. In a general procedure, a stock solution of ~ 2.0 mM $[LCu^{I}(MeCN)]B(C_6F_5)_4$ [L= tmpa] is made by dissolving the solid complexes in EtOH (or MeOH) in scintillation vials in the glovebox. Each LCu solution was transferred in a Schlenk cuvette via syringe, capped with septum, parafilmed and taken out of the glovebox. The cuvette is allowed to cool to −110 ^{0}C (for EtOH) or −90 ^{0}C (for MeOH) in the cryostat of the UV-Vis spectrophotometer for 15 minutes and then 5.0 ml of $^{14}N^{16}O_{(g)}$ is injected at once through a metallic needle of a 3-way gastight syringe following which the spectra are recorded. The same procedure is followed for recording the spectra at −50 ^{0}C corresponding to Figure 4. A 5.0 ml 3-way gastight syringe, prevacuum/$Ar_{(g)}$ purged and equipped with a long (10-inch, 21-gauge) needle, was used to transfer the gas to a reaction vessel by drawing up gas from the Schlenk flask headspace.

Resonance Raman Spectroscopy. Resonance Raman samples were prepared inside a glovebox containing less than 1 ppm O_2 (Omnilab System, Vacuum Atmospheres Co.) as ~2.0 mM stock solution of $[(tmpa)Cu(MeCN)]B(C_6F_5)_4$ (***1***) in EtOH or MeTHF:THF mixture; 500 μl aliquots were transferred to standard NMR tubes and capped with tightfitting septa and parafilm wrapping. The sample tubes were placed in a cold bath (EtOH/liq N_2 (−110 °C)) and maintained at -110 °C for 10 minutes before a fast, one-time addition of 5 ml $NO_{(g)}$ with a gastight Hamilton syringe previously loaded with unlabeled or labeled gas inside the glovebox. The mixture was allowed to react at −110 °C for ~2 hours and frozen in liquid N_2.

Resonance Raman samples were obtained using a custom McPherson 2061/207 spectrometer equipped with a Princeton Instrument liquid-N_2-cooled CCD detector (LN-1100 PB). Semrock RazorEdge filters were used to attenuate Rayleigh scattering. Excitations were from a krypton or argon ion laser (Innova 302C and Innova 90, Coherent). Laser intensities ranged from 5 to 20 mW and were loosely focused with a cylindrical lens to illuminate an area of 10 mm by 0.2 mm at the bottom of the sample in the NMR tube. The NMR tube was maintained at ~110 K inside a copper cold finger cooled with liquid nitrogen and was spun continuous to minimize photochemistry and bleaching of chromophoric complexes. Frequencies were calibrated relative to aspirin and are accurate to ± 1 cm^{-1}.

Electron Paramagnetic Resonance (EPR) Spectroscopy. In the glovebox, a 500 μl of 2.0 mM solution of $[(tmpa)Cu(MeCN)]B(C_6F_5)_4$ (***1***) in EtOH was prepared, transferred to an EPR tube and capped with tightfitting septa before parafilmed. The sample tube was placed in a cold bath (EtOH/liq N_2 (−110 °C)) and maintained at that temperature for 10 minutes before a fast, one-time addition of 5 ml $^{14}N^{16}O_{(g)}$ via a fine-point needle of a three-way gastight syringe. The mixture was allowed to react at −110 °C for ~2 hours prior to the tube being frozen in liquid N_2. Figure 7 depicts the EPR data obtained.

ASSOCIATED CONTENT

Supporting Information. Stopped flow kinetic analyses, UV–Vis spectra, Computational analyses, Gas chromatograms and methodologies; this material is available free of charge via the Internet at http://pubs.acs.org.

AUTHOR INFORMATION

Corresponding Author

karlin@jhu.edu
moennelo@ohsu.edu
mbhadra@mit.edu

ORCID

Mayukh Bhadra: 0000-0002-4758-1610

Therese Albert: 0000-0001-7248-0873

Alicja Franke: 0000-0002-6318-7429

Ivana Ivanović-Burmazović: 0000-0002-1651-3359

Marcel Swart: 0000-0002-8174-8488

Pierre Moenne-Loccoz: 0000-0002-7684-7617

Kenneth D. Karlin: 0000-0002-5675-7040

Present Address

[§]Department of Chemistry, Massachusetts Institute of Technology, Cambridge, Massachusetts 02139, USA

Author Contributions

The manuscript was written through contributions of all authors. All authors have given approval to the final version of the manuscript. The authors declare no competing financial interest.

Funding Sources

This research was supported by the National Institutes of Health and the Spanish ministry of Science, the Bayerisches Staatsministerium für Wissenschaft und Kunst and the appropriate grants are gracefully

acknowledged (GM28962 to K.D.K.; GM74785 to P.M.L. and CTQ2017-87392-P/PID2020-114548GB-I00 to M.S.)

ACKNOWLEDGMENT

This research was supported by the USA National Institutes of Health and the authors acknowledge the funding from all sources mentioned above. The contents of this publication are solely the responsibility of the authors and do not necessarily represent the official views of NIH or the aforesaid scientific bodies. The authors acknowledge the usage of the EPR instrument housed in the Department of Instrumentation Facility (DCIF) of the Department of Chemistry at MIT for experiments during revision of the manuscript.

REFERENCES

(1) Ignarro, L. J. Biosynthesis and Metabolism of Endothelium-Derived Nitric Oxide. *Annu. Rev. Pharmacol. Toxicol.* **1990,** *30,* 535-560.

(2) Ignarro, L. J. Nitric Oxide as a Communication Signal in Vascular and Neuronal Cells. *Nitric Oxide,* Lancaster, J., Ed. Academic Press: San Diego, **1996**; 111-137.

(3) Tennyson, A. G.; Lippard, S. J. Generation, Translocation, and Action of Nitric Oxide in Living Systems. *Chem. Biol.* **2011,** *18,* 1211-1220.

(4) Toledo, J. C.; Augusto, O. Connecting the Chemical and Biological Properties of Nitric Oxide. *Chem. Res. Toxicol.* **2012,** *25,* 975-989.

(5) Hu, K.; Li, Y.; Rotenberg, S. A.; Amatore, C.; Mirkin, M. V. Electrochemical Measurements of Reactive Oxygen and Nitrogen Species inside Single Phagolysosomes of Living Macrophages. *J. Am. Chem. Soc.* **2019,** *141,* 4564-4568.

(6) Pacher, P.; Beckman, J. S.; Liaudet, L. Nitric Oxide and Peroxynitrite in Health and Disease. *Physiol. Rev.* **2007,** *87,* 315-424.

(7) Ferrer-Sueta, G.; Campolo, N.; Trujillo, M.; Bartesaghi, S.; Carballal, S.; Romero, N.; Alvarez, B.; Radi, R. Biochemistry of Peroxynitrite and Protein Tyrosine Nitration. *Chem. Rev.* **2018,** *118,* 1338-1408.

(8) Szabó, C.; Ischiropoulos, H.; Radi, R. Peroxynitrite: Biochemistry, Pathophysiology and Development of Therapeutics. *Nat. Rev. Drug Discov.* **2007,** *6,* 662-680.

(9) Radi, R. Protein Tyrosine Nitration: Biochemical Mechanisms and Structural Basis of Functional Effects. *Acc. Chem. Res.* **2013,** *46,* 550-559.

(10) Barry, S. M.; Kers, J. A.; Johnson, E. G.; Song, L.; Aston, P. R.; Patel, B.; Krasnoff, S. B.; Crane, B. R.; Gibson, D. M.; Loria, R.; Challis, G. L. Cytochrome P450–catalyzed L-tryptophan Nitration in Thaxtomin Phytotoxin Biosynthesis. *Nat. Chem. Biol.* **2012,** *8,* 814-816.

(11) Ye, H.; Li, H.; Gao, Z. Copper Binding Induces Nitration of NPY under Nitrative Stress: Complicating the Role of NPY in Alzheimer's Disease. *Chem. Res. Toxicol.* **2018,** *31,* 904-913.

(12) Fujii, S.; Sawa, T.; Ihara, H.; Tong, K. I.; Ida, T.; Okamoto, T.; Ahtesham, A. K.; Ishima, Y.; Motohashi, H.; Yamamoto, M., Akaike, T. The Critical Role of Nitric Oxide Signaling, via Protein S-Guanylation and Nitrated Cyclic GMP, in the Antioxidant Adaptive Response. *J. Biol. Chem.* **2010,** *285,* 23970-23984.

(13) Schopfer, M. P.; Wang, J.; Karlin, K. D. Bioinspired Heme, Heme/Nonheme Diiron, Heme/Copper, and Inorganic NOx Chemistry: $^{\bullet}NO_{(g)}$ Oxidation, Peroxynitrite–Metal Chemistry, and $\bullet NO(g)$ Reductive Coupling. *Inorg. Chem.* **2010,** *49* , 6267-6282.

(14) Kurtz, J. D. M. Flavo-diiron enzymes: Nitric oxide or Dioxygen Reductases? *Dalton Trans.* **2007**, 4115-4121.

(15) Kumita, H.; Matsuura, K.; Hino, T.; Takahashi, S.; Hori, H.; Fukumori, Y.; Morishima, I.; Shiro, Y. NO Reduction by Nitric-oxide Reductase from Denitrifying Bacterium Pseudomonas aeruginosa Characterization of Reaction Intermediates that appear in the Single Turnover Cycle. *J. Biol. Chem.* **2004,** *279,* 55247-55254.

(16) Shiro, Y. Structure and Function of Bacterial Nitric oxide Reductases: Nitric oxide Reductase, Anaerobic Enzymes. *Biochim. Biophys. Acta. Bioenerg BBA* **2012,** *1817,* 1907-1913.

(17) Hayashi, T.; Lin, M. T.; Ganesan, K.; Chen, Y.; Fee, J. A.; Gennis, R. B.; Moënne-Loccoz, P. Accommodation of Two Diatomic Molecules in Cytochrome bo_3: Insights into NO Reductase Activity in Terminal Oxidases. *Biochemistry* **2009,** *48,* 883-890.

(18) Wasser, I. M.; de Vries, S.; Moënne-Loccoz, P.; Schröder, I.; Karlin, K. D. Nitric Oxide in Biological Denitrification: Fe/Cu Metalloenzyme and Metal Complex NOx Redox Chemistry. *Chem. Rev.* **2002,** *102,* 1201-1234.

(19) Silaghi-Dumitrescu, R.; Kurtz, D. M.; Ljungdahl, L. G.; Lanzilotta, W. N. X-ray Crystal Structures of Moorella thermoacetica FprA. Novel Diiron Site Structure and Mechanistic Insights into a Scavenging Nitric Oxide Reductase. *Biochemistry* **2005,** *44,* 6492-6501.

(20) Lu, J.; Bi, B.; Lai, W.; Chen, H. Origin of Nitric Oxide Reduction Activity in Flavo–Diiron NO Reductase: Key Roles of the Second Coordination Sphere. *Angew. Chem. Int. Ed. Engl.* **2019,** *58,* 3795-3799.

(21) Caranto, J. D.; Weitz, A.; Hendrich, M. P.; Kurtz, D. M. The Nitric Oxide Reductase Mechanism of a Flavo-Diiron Protein: Identification of Active-Site Intermediates and Products. *J. Am. Chem. Soc.* **2014,** *136,* 7981-7992.

(22) Weitz, A. C.; Giri, N.; Frederick, R. E.; Kurtz, D. M.; Bominaar, E. L.; Hendrich, M. P. Spectroscopy and DFT Calculations of Flavo–Diiron Nitric Oxide Reductase Identify Bridging Structures of NO-Coordinated Diiron Intermediates. *ACS Catal.* **2018,** *8,* 11704-11715.

(23) Lehnert, N.; Kim, E.; Dong, H. T.; Harland, J. B.; Hunt, A. P.; Manickas, E. C.; Oakley, K. M.; Pham, J.; Reed, G. C.; Alfaro, V. S. The Biologically Relevant Coordination Chemistry of Iron and Nitric Oxide: Electronic Structure and Reactivity. *Chem. Rev.* **2021,** *121,* 14682-14905.

(24) Lehnert, N.; Dong, H. T.; Harland, J. B.; Hunt, A. P.; White, C. J. Reversing nitrogen fixation. *Nat. Rev. Chem.* **2018,** *2,* 278-289.

(25) Lancaster, K. M.; Caranto, J. D.; Majer, S. H.; Smith, M. A. Alternative Bioenergy: Updates to and Challenges in Nitrification Metalloenzymology. *Joule* **2018,** *2,* 421-441.

(26) Granger, P.; Parvulescu, V. I. Catalytic NOx Abatement Systems for Mobile Sources: From Three-Way to Lean Burn after-Treatment Technologies. *Chem. Rev.* **2011,** *111,* 3155-3207.

(27) Gao, F.; Mei, D.; Wang, Y.; Szanyi, J.; Peden, C. H. F. Selective Catalytic Reduction over Cu/SSZ-13: Linking Homo and Heterogeneous Catalysis. *J. Am. Chem. Soc.* **2017,** *139,* 4935-4942.

(28) Mohiuddin, A. K. M. Development of Catalytic Converter Using Non-Precious Metals. *Adv. Mat. Res.* **2015,** *1115,* 462-467.

(29) Moënne-Loccoz, P. Spectroscopic Characterization of Heme Iron–nitrosyl Species and their Role in NO Reductase Mechanisms in Diiron Proteins. *Nat. Prod. Rep.* **2007,** *24,* 610-620.

(30) Pinakoulaki, E.; Varotsis, C. Nitric oxide Activation and Reduction by Heme–Copper Oxidoreductases and Nitric oxide Reductase. *J. Inorg. Biochem.* **2008,** *102,* 1277-1287.

(31) Forte, E.; Urbani, A.; Saraste, M.; Sarti, P.; Brunori, M.; Giuffre, A. The Cytochrome cbb_3 from *Pseudomonas stutzeri* displays Nitric oxide Reductase Activity. *Eur. J. Biochem.* **2001,** *268,* 6486-6491.

(32) Giuffre, A.; Stubauer, G.; Sarti, P.; Brunori, M.; Zumft, W. G.; Buse, G.; Soulimane, T. The Heme-Copper Oxidases of *Thermus thermophilus* Catalyze the Reduction of Nitric oxide: Evolutionary Implications. *Proc. Natl. Acad. Sci. U.S.A.* **1999,** *96,* 14718-14723.

(33) Hayashi, T.; Lin, I. J.; Chen, Y.; Fee, J. A.; Moënne-Loccoz, P. Fourier Transform Infrared Characterization of a Cu_B–Nitrosyl Complex in Cytochrome ba_3 from Thermus thermophilus: Relevance to NO Reductase Activity in Heme–Copper Terminal Oxidases. *J. Am. Chem. Soc.* **2007,** *129,* 14952-14958.

(34) Hayashi, T.; Lin, M. T.; Ganesan, K.; Chen, Y.; Fee, J. A.; Gennis, R. B.; Moënne-Loccoz, P. Accommodation of Two Diatomic Molecules in Cytochrome bo_3: Insights into NO Reductase Activity in Terminal Oxidases. *Biochemistry* **2009,** *48,* 883-890.

(35) Ohta, T.; Soulimane, T.; Kitagawa, T.; Varotsis, C. Nitric oxide Activation by caa_3 oxidoreductase from Thermus thermophilus. *Phys. Chem. Chem. Phys.* **2015,** *17,* 10894-10898.

(36) Hayashi, T.; Caranto, J. D.; Matsumura, H.; Kurtz, D. M., Jr.; Moënne-Loccoz, P. Vibrational Analysis of Mononitrosyl Complexes in Hemerythrin and Flavodiiron Proteins: Relevance to Detoxifying NO Reductase. *J. Am. Chem. Soc.* **2012,** *134,* 6878-6884.

(37) Hayashi, T.; Caranto, J. D.; Wampler, D. A.; Kurtz, D. M.; Moënne-Loccoz, P. Insights into the Nitric Oxide Reductase Mechanism of Flavodiiron Proteins from a Flavin-Free Enzyme. *Biochemistry* **2010,** *49,* 7040-7049.

(38) Khatua, S.; Majumdar, A. Flavodiiron Nitric oxide Reductases: Recent Developments in the Mechanistic Study and Model Chemistry for the Catalytic Reduction of NO. *J. Inorg. Biochem.* **2015,** *142,* 145-153.

(39) Shoun, H.; Fushinobu, S.; Jiang, L.; Kim, S. W.; Wakagi, T. Fungal Denitrification and Nitric oxide Reductase Cytochrome P450nor. *Philos. Trans. R. Soc. Lond., B, Biol. Sci.* **2012,** *367,* 1186-1194.

(40) Obayashi, E.; Takahashi, S.; Shiro, Y. Electronic Structure of Reaction Intermediate of Cytochrome P450nor in Its Nitric Oxide Reduction. *J. Am. Chem. Soc.* **1998,** *120,* 12964-12965.

(41) Nomura, T.; Kimura, T.; Kanematsu, Y.; Yamada, D.; Yamashita, K.; Hirata, K.; Ueno, G.; Murakami, H.; Hisano, T.; Yamagiwa, R.; Takeda, H.; Gopalasingam, C.; Kousaka, R.; Yanagisawa, S.; Shoji, O.; Kumasaka, T.; Yamamoto, M.; Takano, Y.; Sugimoto, H.; Tosha, T.; Kubo, M.; Shiro, Y. Short-lived Intermediate in N_2O generation by P450 NO Reductase Captured by Time-resolved IR Spectroscopy and XFEL Crystallography. *Proc. Natl. Acad. Sci. U. S. A.* **2021,** *118,* e2101481118.

(42) White, C. J.; Speelman, A. L.; Kupper, C.; Demeshko, S.; Meyer, F.; Shanahan, J. P.; Alp, E. E.; Hu, M.; Zhao, J.; Lehnert, N. The Semireduced Mechanism for Nitric Oxide Reduction by Non-Heme Diiron Complexes: Modeling Flavodiiron Nitric Oxide Reductases. *J. Am. Chem. Soc.* **2018,** *140,* 2562-2574.

(43) Van Stappen, C.; Lehnert, N. Mechanism of N–N Bond Formation by Transition Metal–Nitrosyl Complexes: Modeling Flavodiiron Nitric Oxide Reductases. *Inorg. Chem.* **2018,** *57,* 4252-4269.

(44) Berto, T. C.; Xu, N.; Lee, S. R.; McNeil, A. J.; Alp, E. E.; Zhao, J.; Richter-Addo, G. B.; Lehnert, N. Characterization of the Bridged Hyponitrite Complex $\{[Fe(OEP)]_2(\mu\text{-}N_2O_2)\}$: Reactivity of Hyponitrite Complexes and Biological Relevance. *Inorg. Chem.* **2014,** *53,* 6398-6414.

(45) Berto, T. C.; Speelman, A. L.; Zheng, S.; Lehnert, N. Mono- and dinuclear Non-heme Iron–nitrosyl Complexes: Models for Key Intermediates in Bacterial Nitric oxide Reductases. *Coord. Chem. Rev.* **2013,** *257,* 244-259.

(46) Dong, H. T.; White, C. J.; Zhang, B.; Krebs, C.; Lehnert, N. Non-Heme Diiron Model Complexes Can Mediate Direct NO Reduction: Mechanistic Insight into Flavodiiron NO Reductases. *J. Am. Chem. Soc.* **2018,** *140,* 13429-13440.

(47) Wright, A. M.; Hayton, T. W. Understanding the Role of Hyponitrite in Nitric Oxide Reduction. *Inorg. Chem.* **2015,** *54,* 9330-9341.

(48) Wu, W.-Y.; Liaw, W.-F. Nitric oxide Reduction forming Hyponitrite triggered by Metal-containing Complexes. *J. Chin. Chem. Soc.* **2020,** *67,* 206-212.

(49) Flock, U.; Reimann, J.; Ädelroth, P. Proton Transfer in Bacterial Nitric oxide Reductase. *Biochem. Soc. Trans.* **2006,** *34,* 188-190.

(50) Hendriks, J. H. M.; Jasaitis, A.; Saraste, M.; Verkhovsky, M. I. Proton and Electron Pathways in the Bacterial Nitric Oxide Reductase. *Biochemistry* **2002,** *41,* 2331-2340.

(51) Yi, J.; Morrow, B. H.; Campbell, A. L. O. C.; Shen, J. K.; Richter-Addo, G. B. Nitric oxide Coupling Mediated by Iron Porphyrins: the N–N Bond Formation Step is Facilitated by Electrons and a Proton. *Chem. Commun.* **2012,** *48,* 9041-9043.

(52) Takeda, H.; Kimura, T.; Nomura, T.; Horitani, M.; Yokota, A.; Matsubayashi, A.; Ishii, S.; Shiro, Y.; Kubo, M.; Tosha, T. Timing of NO Binding and Protonation in the Catalytic Reaction of Bacterial Nitric Oxide Reductase as Established by Time-Resolved Spectroscopy. *Bull. Chem. Soc. Jpn.* **2020,** *93,* 825-833.

(53) (a) Ruggiero, C. E.; Carrier, S. M.; Antholine, W. E.; Whittaker, J. W.; Cramer, C. J.; Tolman, W. B *J. Am. Chem. Soc.* **1993,** *115,* 11285-11298 (b) Ruggiero, C. E.; Carrier, S. M.; Tolman, W. B. Reductive Disproportionation of NO Mediated by Copper Complexes: Modeling N_2O Generation by Copper Proteins and Heterogeneous Catalysts. *Angew. Chem. Int. Ed. Engl.* **1994,** *33,* 895-897. (c) Schneider, J. L.; Carrier, S. M.; Ruggiero, C. E.; Young, V. G.; Tolman, W. B. Influences of Ligand Environment on the Spectroscopic Properties and Disproportionation Reactivity of Copper–Nitrosyl Complexes. *J. Am. Chem. Soc.* **1998,** *120,* 11408-11418.

(54) Fujisawa, K.; Tateda, A.; Miyashita, Y.; Okamoto, K.; Paulat, F.; Praneeth, V. K. K.; Merkle, A.; Lehnert, N. *J. Am. Chem. Soc.* **2008,** *130,* 1205-1213.

(55) (a) Usov, O. M.; Sun, Y.; Grigoryants, V. M.; Shapleigh, J. P.; Scholes, C. P. *J. Am. Chem. Soc.* **2006,** *128,* 13102-13111 (b) Ghosh, S.; Dey, A.; Usov, O. M.; Sun, Y.; Grigoryants, V. M.; Scholes, C. P.; Solomon, E. I. *J. Am. Chem. Soc.* **2007,** *129,* 10310-10311.

(56) Shimokawabe, M.; Okumura, K.; Ono, H.; Takezawa, N. N_2O and NO_2 Formation in the Disproportionation of NO over Ion Exchanged Cu-ZSM-5 at Lower Temperature. *React. Kinet. Catal. Lett.* **2001,** *73,* 267-274.

(57) Metz, S. N_2O Formation via Reductive Disproportionation of NO by Mononuclear Copper Complexes: A Mechanistic DFT Study. *Inorg. Chem.* **2017,** *56,* 3820-3833.

(58) (a) Wright, A. M.; Sun, C.; Dincă, M. Thermal Cycling of a MOF-Based NO Disproportionation Catalyst. *J. Am. Chem. Soc.* **2021,** *143,* 681-686 (b) Sun, C.; Yang, L.; Ortuño, M. A.; Wright, A. M.; Chen, T.; Head, A. R.; López, N.; Dincă, M. Spectroscopic Evidence of Hyponitrite Radical Intermediate in NO Disproportionation at a MOF-Supported Mononuclear Copper Site. *Angew. Chem. Int. Ed. Engl.* **2021,** *60,* 7845-7850.

(59) Cao, R.; Elrod, L. T.; Lehane, R. L.; Kim, E.; Karlin, K. D. A Peroxynitrite Dicopper Complex: Formation via Cu–NO and Cu–O_2 Intermediates and Reactivity via O–O Cleavage Chemistry. *J. Am. Chem. Soc.* **2016,** *138,* 16148-16158.

(60) Liu, J. J.; Siegler, M. A.; Karlin, K. D.; Moënne-Loccoz, P. Direct Resonance Raman Characterization of a Peroxynitrito Copper Complex Generated from O_2 and NO and Mechanistic Insights into Metal-Mediated Peroxynitrite Decomposition. *Angew. Chem. Int. Ed. Engl.* **2019,** *58,* 10936-10940.

(61) Martínez-Ahumada, E.; Díaz-Ramírez, M. L.; Velásquez-Hernández, M. d. J.; Jancik, V.; Ibarra, I. A. Capture of Toxic Gases in MOFs: SO_2, H_2S, NH_3 and NOx. *Chem. Sci.* **2021,** *12,* 6772-6799.

(62) Wijeratne, G. B.; Hematian, S.; Siegler, M. A.; Karlin, K. D. Copper(I)/$NO_{(g)}$ Reductive Coupling Producing a trans-Hyponitrite Bridged Dicopper(II) Complex: Redox Reversal Giving Copper(I)/$NO_{(g)}$ Disproportionation. *J. Am. Chem. Soc.* **2017,** *139,* 13276-13279.

(63) Xu, N.; Campbell, A. L. O.; Powell, D. R.; Khandogin, J.; Richter-Addo, G. B. A Stable Hyponitrite-Bridged Iron Porphyrin Complex. *J. Am. Chem. Soc.* **2009,** *131,* 2460-2461.

(64) Wu, W.-Y.; Hsu, C.-N.; Hsieh, C.-H.; Chiou, T.-W.; Tsai, M.-L.; Chiang, M.-H.; Liaw, W.-F. NO-to-$[N_2O_2]^{2-}$-to-N_2O Conversion Triggered by $\{Fe(NO)_2\}^{10}$-$\{Fe(NO)_2\}^9$ Dinuclear Dinitrosyl Iron Complex. *Inorg. Chem.* **2019,** *58,* 9586-9591.

(65) Liu, P.-H.; Tsai, F.-T.; Chen, B.-H.; Hsu, I.-J.; Hsieh, H.-H.; Liaw, W.-F. Insight Into Chalcogenolate-bound $\{Fe(NO)_2\}^9$ Dinitrosyl Iron Complexes (DNICs): Covalent Character Versus Ionic Character. *Dalton Trans.* **2019,** *48,* 6040-6050.

(66) Bau, R.; Sabherwal, I.; Burg, A. Preparation and Structure of $Co_4(NO)_8(NO_2)_2(N_2O_2)$. Novel Complex Containing a Quadridentate Hyponitrite group. *J. Am. Chem. Soc.* **1971,** *93,* 4926-4928.

(67) Evans, W. J.; Fang, M.; Bates, J. E.; Furche, F.; Ziller, J. W.; Kiesz, M. D.; Zink, J. I. Isolation of a Radical Dianion of Nitrogen oxide $(NO)^{2-}$. *Nat. Chem.* **2010,** *2,* 644-647.

(68) Lionetti, D.; de Ruiter, G.; Agapie, T. A trans-Hyponitrite Intermediate in the Reductive Coupling and Deoxygenation of Nitric Oxide by a Tricopper–Lewis Acid Complex. *J. Am. Chem. Soc.* **2016,** *138,* 5008-5011.

(69) Arikawa, Y.; Asayama, T.; Moriguchi, Y.; Agari, S.; Onishi, M. Reversible N–N Coupling of NO Ligands on Dinuclear Ruthenium Complexes and Subsequent N_2O Evolution: Relevance to Nitric Oxide Reductase. *J. Am. Chem. Soc.* **2007,** *129,* 14160-14161.

(70) Kundu, S.; Phu, P. N.; Ghosh, P.; Kozimor, S. A.; Bertke, J. A.; Stieber, S. C. E.; Warren, T. H. Nitrosyl Linkage Isomers: NO Coupling to N_2O at a Mononuclear Site. *J. Am. Chem. Soc.* **2019,** *141,* 1415-1419.

(71) Wright, A. M.; Wu, G.; Hayton, T. W. Formation of N_2O from a Nickel Nitrosyl: Isolation of the cis-$[N_2O_2]^{2-}$ Intermediate. *J. Am. Chem. Soc.* **2012,** *134,* 9930-9933.

(72) Wright, A. M.; Zaman, H. T.; Wu, G.; Hayton, T. W. Mechanistic Insights into the Formation of N_2O by a Nickel Nitrosyl Complex. *Inorg. Chem.* **2014,** *53,* 3108-3116.

(73) Ferretti, E.; Dechert, S.; Demeshko, S.; Holthausen, M. C.; Meyer, F. Reductive Nitric Oxide Coupling at a Dinickel Core: Isolation of a Key cis-Hyponitrite Intermediate en route to N_2O Formation. *Angew. Chem. Int. Ed. Engl.* **2019,** *58,* 1705-1709.

(74) Ghosh, P.; Stauffer, M.; Hosseininasab, V.; Kundu, S.; Bertke, J. A.; Cundari, T. R.; Warren, T. H. *J. Am. Chem. Soc.* **2022**, 144, 15093-15099.

(75) Wijeratne, G. B.; Bhadra, M.; Siegler, M. A.; Karlin, K. D. Copper(I) Complex Mediated Nitric Oxide Reductive Coupling: Ligand Hydrogen Bonding Derived Proton Transfer Promotes $N_2O_{(g)}$ Release. *J. Am. Chem. Soc.* **2019,** *141,* 17962-17967..

(76) Tsai, M.-L.; Tsou, C.-C.; Liaw, W.-F. Dinitrosyl Iron Complexes (DNICs): From Biomimetic Synthesis and Spectroscopic Characterization Toward Unveiling the Biological and Catalytic Roles of DNICs. *Acc. Chem. Res.* **2015,** *48,* 1184-1193.

(77) Dai, R. J.; Ke, S. C. Detection and Determination of the $\{Fe(NO)_2\}$ Core Vibrational Features in Dinitrosyl–Iron Complexes from Experiment, Normal Coordinate Analysis, and Density Functional Theory: An Avenue for Probing the Nitric Oxide Oxidation State. *J. Phys. Chem. B.* **2007,** *111,* 2335-2346.

(78) Iwamoto, M.; Yahiro, H.; Mizuno, N.; Zhang, W. X.; Mine, Y.; Furukawa, H.; Kagawa, S. Removal of Nitrogen monoxide Through a Novel Catalytic Process. 2. Infrared study on Surface Reaction of Nitrogen monoxide Adsorbed on Copper Ion-exchanged ZSM-5 Zeolites. *J. Phys. Chem.* **1992,** *96,* 9360-9366.

(79) (a) Shelef, M. Selective Catalytic Reduction of NOx with N-Free Reductants. *Chem. Rev.* **1995,** *95,* 209-225. (b) Ruschel, G. K.; Nemetz, T. M.; Ball, D. W. Matrix Isolation and Density Functional Studies of Novel Transition Metal Complexes. NO + Fe, Co, Ni, Cu, and Zn in Argon Matrices. *J. Mol. Struct.* **1996,** *384,* 101-114.

(80) As expected for a dinitrosyl Cu-$(NO)_2$ species, EPR spectroscopy indicates a diamagnetic behavior (see the SI).

(81) Kuhn, L.; Lippincott, E. R. The Vibrational Spectrum and Structure of the Hyponitrite Ion. *J. Am. Chem. Soc.* **1956,** *78,* 1820-1821.

(82) Villalba, M. E. C.; Navaza, A.; Güida, J. A.; Varetti, E. L.; Aymonino, P. J. New Structural Study and Reinterpretation of the Vibrational Spectra of the μ-N,O-hyponitrite bis[pentaamminecobalt(III)]$^{4+}$ cation. *Inorg. Chim. Acta* **2006,** *359,* 707-712.

(83) Walker, F. A.; Lo, M.-W.; Ree, M. T. Electronic Effects in Transition Metal Porphyrins. The Reactions of Imidazoles and Pyridines with a Series of Para-substituted Tetraphenylporphyrin Complexes of Chloroiron(III). *J. Am. Chem. Soc.* **1976,** *98,* 5552-5560.

(84) Kim, Y. O.; Goff, H. M. Characterization of Ammonia-ligated Low-spin Iron(III) Porphyrin Complexes. *Inorg. Chem.* **1990,** *29,* 3907-3908.

(85) La Mar, G. N.; Walker, F. A. Dynamics of Axial Ligation in Metalloporphyrins. I. Imidazole Exchange in Low-spin Ferric Porphyrins. *J. Am. Chem. Soc.* **1972,** *94,* 8607-8608.

(86) Balke, V. L.; Walker, F. A.; West, J. T. Electronic Effects in Transition-metal Porphyrins. 6. The Effect of Unsymmetrical Phenyl Substitution on the Formation Constants of a Series of (tetraphenylporphinato)iron(III)-bis(N-methylimidazole) Complexes. *J. Am. Chem. Soc.* **1985,** *107,* 1226-1233.

(87) Oszajca, M.; Drzewiecka-Matuszek, A.; Franke, A.; Rutkowska-Zbik, D.; Brindell, M.; Witko, M.; Stochel, G.; van Eldik, R. Mechanistic Insight into Peroxo-Shunt Formation of Biomimetic Models for Compound II, Their Reactivity toward Organic Substrates, and the Influence of N-Methylimidazole Axial Ligation. *Eur. J. Chem.* **2014,** *20,* 2328-2343.

(88) Swart, M. A New Family of Hybrid Density Functionals. *Chem. Phys. Lett.* **2013,** *580,* 166-171.

(89) Swart, M.; Gruden, M. Spinning around in Transition-Metal Chemistry. *Acc. Chem. Res.* **2016,** *49,* 2690-2697.

(90) Banerjee, S.; Draksharapu, A.; Crossland, P. M.; Fan, R.; Guo, Y.; Swart, M.; Que, L. Sc^{3+}-Promoted O–O Bond Cleavage of a (μ-1,2-Peroxo)diiron(III) Species Formed from an Iron(II) Precursor and O_2 to Generate a Complex with an $Fe^{IV}_2(\mu\text{-}O)_2$ Core. *J. Am. Chem. Soc.* **2020,** *142,* 4285-4297.

(91) Martins, F.F.; Swart. M. Coupled Cluster and Density Functional Approaches for Proton Affinity and Basicity, a Benchmark Study. *Phys. Chem. Chem. Phys.*, manuscript in preparation, to be submitted.

(92) Walroth, R. C.; Lukens, J. T.; MacMillan, S. N.; Finkelstein, K. D.; Lancaster, K. M. Spectroscopic Evidence for a $3d^{10}$ Ground State Electronic Configuration and Ligand Field Inversion in $[Cu(CF_3)_4]^{1-}$. *J. Am. Chem. Soc.* **2016,** *138,* 1922-1931.

(93) (a) Tao, W.; Carter, S.; Trevino, R.; Zhang, W.; Shafaat, H. S.; Zhang, S. *J. Am. Chem. Soc.* **2022,** *144,* 22633-22640. (b) Dong, H. T.; Speelman, A. L.; Kozemchak, C. E.; Sil, D.; Krebs, C.; Lehnert, N. The

$Fe_2(NO)_2$ Diamond Core: A Unique Structural Motif In Non-Heme Iron–NO Chemistry. *Angew. Chem. Int. Ed. Engl.* **2019,** *58*, 17695-17699.

(94) Chuang, C.-H.; Liaw, W.-F.; Hung, C.-H. Conversion of Nitric Oxide into Nitrous Oxide as Triggered by the Polarization of Coordinated NO by Hydrogen Bonding. *Angew. Chem. Int. Ed. Engl.* **2016,** *55*, 5190-5194.

(95) Schopfer, M. P.; Mondal, B.; Lee, D.-H.; Sarjeant, A. A. N.; Karlin, K. D. Heme/O_2/•NO Nitric Oxide Dioxygenase (NOD) Reactivity: Phenolic Nitration via a Putative Heme-Peroxynitrite Intermediate. *J. Am. Chem. Soc.* **2009,** *131*, 11304-11305.

(96) Wang, J.; Schopfer, M. P.; Sarjeant, A. A. N.; Karlin, K. D. Heme-Copper Assembly Mediated Reductive Coupling of Nitrogen Monoxide (•NO). *J. Am. Chem. Soc.* **2009,** *131*, 450-451.

(97) Ford, P. C.; Lorkovic, I. M. Mechanistic Aspects of the Reactions of Nitric Oxide with Transition-Metal Complexes. *Chem. Rev.* **2002,** *102*, 993-1018.

(98) Jee, J.-E.; Eigler, S.; Hampel, F.; Jux, N.; Wolak, M.; Zahl, A.; Stochel, G.; van Eldik, R. Kinetic and Mechanistic Studies on the Reaction of Nitric Oxide with a Water-Soluble Octa-anionic Iron(III) Porphyrin Complex. *Inorg. Chem.* **2005,** *44*, 7717-7731.

(99) Baerends, E. J.; Ziegler, T.; Autschbach, J.; Bashford, D.; Berger, A.; Bérces, A.; Bickelhaupt, F. M.; Bo, C.; de Boeij, P. L.; Boerrigter, P. M.; Borini, S.; Bulo, R. E.; Cavallo, L.; Chong, D. P.; Deng, L.; Dickson, R. M.; van Duin, A. C. T.; Ellis, D. E.; Faassen, M. v.; Fan, L.; Fischer, T. H.; Fonseca Guerra, C.; Ghysels, A.; Giammona, A.; van Gisbergen, S. J. A.; Götz, A. W.; Groeneveld, J. A.; Gritsenko, O. V.; Grüning, M.; Gusarov, S.; Harris, F. E.; Heine, T.; van den Hoek, P.; Jacob, C. R.; Jacobsen, H.; Jensen, L.; Kadantsev, E. S.; Kaminski, J. W.; van Kessel, G.; Klooster, R.; Kootstra, F.; Kovalenko, A.; Krykunov, M. V.; van Lenthe, E.; Louwen, J. N.; McCormack, D. A.; McGarrity, E.; Michalak, A.; Mitoraj, M.; Neugebauer, J.; Nicu, V. P.; Noodleman, L.; Osinga, V. P.; Patchkovskii, S.; Philipsen, P. H. T.; Post, D.; Pye, C. C.; Ravenek, W.; Rodríguez, J. I.; Romaniello, P.; Ros, P.; Schipper, P. R. T.; Schreckenbach, G.; Seldenthuis, J. S.; Seth, M.; Skachkov, D. G.; Snijders, J. G.; Solà, M.; Swart, M.; Swerhone, D.; te Velde, G.; Vernooijs, P.; Versluis, L.; Visscher, L.; Visser, O.; Wang, F.; Wesolowski, T. A.; van Wezenbeek, E. M.; Wiesenekker, G.; Wolff, S. K.; Woo, T. K.; Yakovlev, A. L. *ADF2012.01*, ADF2012.01; SCM: Amsterdam, **2012**.

(100) te Velde, G.; Bickelhaupt, F. M.; Baerends, E. J.; Fonseca Guerra, C.; van Gisbergen, S. J. A.; Snijders, J. G.; Ziegler, T. Chemistry with ADF. *J. Comput. Chem.* **2001,** *22*, 931-967.

(101) Swart, M.; Bickelhaupt, F. M. QUILD: QUantum-regions Interconnected by Local Descriptions. *J. Comput. Chem.* **2008,** *29*, 724-734.

(102) van Lenthe, E.; Baerends, E. J. Optimized Slater-Type Basis Sets for the Elements 1–118. *J. Comput. Chem.* **2003,** *24*, 1142-1156.

(103) Chong, D. P.; van Lenthe, E.; van Gisbergen, S. J. A.; Baerends, E. J. Even-tempered Slater-type Orbitals Revisited: From Hydrogen to Krypton. *J. Comput. Chem.* **2004,** *25*, 1030-1036.

(104) Wolff, S. K. Analytical Second Derivatives in the Amsterdam Density Functional Package. *Int. J. Quantum Chem.* **2005,** *104*, 645-659.

(105) Klamt, A.; Schüürmann, G. COSMO: A New Approach to Dielectric Screening in Solvents with Explicit Expressions for the Screening Energy and its Gradient. *J. Chem. Soc., Perkin trans. II* **1993**, 799-805.

(106) Swart, M.; Rösler, E.; Bickelhaupt, F. M. Proton Affinities in Water of Maingroup-Element Hydrides. Effects of Hydration and Methyl Substitution. *Eur. J. Inorg. Chem.* **2007**, 3646-3654.

(107) Averkiev, B. B.; Truhlar, D. G. Free energy of reaction by density functional theory: oxidative addition of ammonia by an iridium complex with PCP pincer ligands. *Catal. Sci. Technol.* **2011,** *1*, 1526-1529.

(108) Klein, J. E. M. N.; Dereli, B.; Que Jr., L.; Cramer, C. J. Why metal–oxos react with dihydroanthracene and cyclohexadiene at comparable rates, despite having different C–H bond strengths. A computational study. *Chem. Commun.* **2016,** *52*, 10509-10512.

(109) van Lenthe, E.; Baerends, E. J.; Snijders, J. G. Relativistic regular two-component Hamiltonians. *J. Chem. Phys.* **1993,** *99*, 4597-4610.

(110) Franchini, M.; Philipsen, P. H. T.; Visscher, L. The Becke Fuzzy Cells Integration Scheme in the Amsterdam Density Functional Program Suite. *J. Comput. Chem.* **2013,** *34*, 1819-1827.

(111) Becke, A. A multicenter numerical integration scheme for polyatomic molecules. *J. Chem. Phys.* **1988,** *88*, 2547-2553.

(112) Wilkinson, M. D.; Dumontier, M.; Aalbersberg, I. J.; Appleton, G.; Axton, M.; Baak, A.; Blomberg, N.; Boiten, J.-W.; da Silva Santos, L. B.; Bourne, P. E.; Bouwman, J.; Brookes, A. J.; Clark, T.; Crosas, M.; Dillo, I.; Dumon, O.; Edmunds, S.; Evelo, C. T.; Finkers, R.; Gonzalez-Beltran, A.; Gray, A. J. G.; Groth, P.; Goble, C.; Grethe, J. S.; Heringa, J.; 't Hoen, P. A. C.; Hooft, R.; Kuhn, T.; Kok, R.; Kok, J.; Lusher, S. J.; Martone, M. E.; Mons, A.; Packer, A. L.; Persson, B.; Rocca-Serra, P.; Roos, M.; van Schaik, R.; Sansone, S.-A.; Schultes, E.; Sengstag, T.; Slater, T.; Strawn, G.; Swertz, M. A.; Thompson, M.; van der Lei, J.; van Mulligen, E.; Velterop, J.; Waagmeester, A.; Wittenburg, P.; Wolstencroft, K.; Zhao, J.; Mons, B. The FAIR Guiding Principles for scientific data management and stewardship. *Sci. Data* **2016,** *3*, 160018.

Insert Table of Contents artwork here